Additive Manufacturing 88 (2024) 104245

Contents lists available at ScienceDirect

Additive Manufacturing

journal homepage: www.elsevier.com/locate/addma

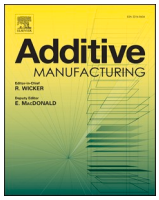

The effect of powder recycling on the mechanical performance of laser powder bed fused stainless steel 316L

Rory Douglas [a], Nicholas Barnard [a], Nicholas Lavery [b], James Sullivan [b], Thomas Jones [c], Robert Lancaster [a,*]

[a] Institute of Structural Materials, Bay Campus, Swansea University, Swansea SA1 8EN, UK
[b] Faculty of Science & Engineering, Bay Campus, Swansea University, Swansea SA1 8EN, UK
[c] Rolls-Royce plc, Kings Place, 90 York Way, London N1 9FX, UK

ARTICLE INFO

Keywords:
Laser powder bed fusion
Powder recycling
Low cycle fatigue
Stainless steel 316L

ABSTRACT

Powder recycling refers to the reuse of unused powder feedstock in the laser powder bed fusion (PBF-LB/M) process. This approach is crucial for the economic viability and sustainability of PBF-LB/M, as powder accounts for a large proportion of the total production cost. However, through powder recycling, the physical and chemical properties of powder are liable to change. This variation in powder properties can subsequently lead to knock-on effects on the mechanical properties of a fully built component.

This research has investigated the changes that occur to stainless steel 316L (SS316L) powder as a result of recycling. This includes changes to powder size distribution (PSD), flowability, chemistry and phase composition. Likewise, the impact that these changes have will also be assessed in PBF-LB/M SS316L components manufactured from powders after different levels of recycling and subjected to alternative post processing routes such as hot isostatic pressing (HIP). This comprehensive investigation involves a thorough examination of both macro- and microstructures, encompassing detailed analyses of chemical composition, microstructural features, and defects. The study aims to elucidate differences in mechanical behaviour through a series of experiments, including uniaxial tensile tests, Charpy impact assessments, and low cycle fatigue (LCF) experiments. Additionally, the investigation will be complemented by pitting potential tests, providing a holistic understanding of the material's performance and characteristics.

Although moderate changes to powder were observed for both PSD and chemistry, this was found to be negligible and not enough to result in any adverse changes to part performance. In addition, the microstructure of SS316L remained stable across differing levels of powder recycling. Whereas the porosity content increased marginally as the fine particle content of powder was reduced, this was not found to be sufficient to affect the LCF performance of the material. After powder recycling, increases in ductility and Young's modulus were attributed to a reduction in oxides present in the microstructure, which were sources of localised damage and deformation.

1. Introduction

Additive manufacturing (AM) methods, including laser powder bed fusion (PBF-LB/M), represent a contemporary manufacturing approach characterised by the melting of metallic powder particles to create intricate components with precise dimensional tolerances [1]. This technique is particularly well-suited for producing small to medium volumes of intricately designed parts, offering the advantage of reducing the need for costly tooling and secondary machining expenses. This attribute makes it particularly appealing to various industries, including the nuclear and aviation sectors. These industries often deal with lower production volumes compared to other sectors, yet demand high engineering complexity and stringent quality control measures.

Much of the earlier investigations on PBF-LB/M have focused on the effect of process parameters on the homogeneity and properties of parts [2–5] and currently, the process is understood well enough to allow for

* Corresponding author.
E-mail addresses: 862472@swansea.ac.uk (R. Douglas), n.c.barnard@swansea.ac.uk (N. Barnard), n.p.lavery@swansea.ac.uk (N. Lavery), j.h.sullivan@swansea.ac.uk (J. Sullivan), thomas.jones2@rolls-royce.com (T. Jones), r.j.lancaster@swansea.ac.uk (R. Lancaster).

https://doi.org/10.1016/j.addma.2024.104245
Received 29 February 2024; Received in revised form 31 May 2024; Accepted 3 June 2024
Available online 8 June 2024

the production of components with densities as high as 99.5–99.9 % [6–8]. In addition, PBF-LB/M of some metals has been shown to lead to comparable and in some situations improved mechanical properties, when compared to their standard wrought material [9,10]. However, PBF-LB/M is still relatively in its infancy when compared to other more traditional manufacturing routes and variations in machine parameters, material chemistry and powder specifications between individual processes mean that this is still a very valid and active area of research.

The understanding of PBF-LB/M has evolved to a point that this manufacturing process is now being used for the production of critical in-service structural components. This success presents new challenges for PBF-LB/M, focussed around optimising the production method in a sustainable way. Included within this is the recyclability of the powder feedstock. In any given build cycle, not all the powder is used to manufacture a single run. Therefore, in theory, the remaining powder can be recycled and reused on consecutive builds. The cost of feedstock material has been reported to represent 31 % of the total cost of PBF-LB/M manufacture so there is a clear benefit for recycling powder to reduce cost, waste and the obvious value in aiding the environment by reducing the carbon footprint required during powder manufacture [11]. Despite these benefits, there is a lack of definitive understanding as to how many times powder can be recycled since the characteristics of powder particles may be altered physically and chemically by recycling and therefore, it may not be appropriate to reuse it indefinitely.

During powder recycling, as the amount of times that powder is recycled increases, there are multiple mechanisms that can lead to changes in the powder properties, which in turn may influence properties of the final PBF-LB/M component. These include spatter particles that may be ejected out of the molten melt pool and lead to the variations in surface chemistry and morphology. Variability in chemistry in particular may be a concern as increases in oxygen content may affect melt pool dynamics and in tun promote porosity [12]. Likewise, irregular morphologies will negatively affect flowability which is important for part processibility [13]. The storage of powder during recycles and multiple builds can also lead to oxygen pickup. Powder storage is not directly linked to recycling powder. However, recycled powder, by definition, will have been used more than fresh virgin powder. Therefore storage of powder throughout its lifecycle when it is not being used could allow for greater oxidation or an increasing moisture content in the powder.

Previous research on PBF-LB/M technologies has aimed to optimise process parameters to achieve maximum densification and minimum porosity within final components [4,14,15]. If changes to the powder feedstock affect the densification of parts, then understanding powder reuse is critical to not undermine the outcomes of previous research in this field. Post processing techniques such as hot isostatic pressing (HIP) may be able to negate these effects fully or partly, which could be a useful tool to have. Historically, HIP operations have been found to reduce the porosity content of PBF-LB/M stainless steel 316 L (SS316L) components to below 1 % [16]. However, this came to the detriment of the resulting tensile properties, where the yield strength significantly reduced, but this was offset by an improved ductility. Given this trade-off and to maximise profitability, the aim should be to minimise post processing as much as possible.

Reviews of the powder evolution of SS316L during multiple recycles of PBF-LB/M have already been completed [17–21]. In fact, the understanding of powder changes during recycling has been relatively well researched, with little evidence of changes to powder morphology, powder size distribution (PSD) or oxygen content of SS316L powders being reported [20]. Douglas et al. [17] documented that when employing an appropriate initial powder specification and sieving during reuse, there is evidence that powder recycling does not significantly and adversely affect the mechanical properties of parts. Notably, the PSD of recycled powder of SS316L and similar stainless steel alloys tends to coarsen, accompanied by an increase in the diameter of fine particles. Likewise, they reported that oxygen content increases with continued recycling, but reported increases have typically remained within standard limits. Changes to the microstructure of recycled SS316L powder have also been observed, with an increase in ferrite content from negligible quantities to 6–7 wt% with increased recycling, despite SS316L having an almost fully austenitic microstructure. Murray et al. [20] observed a similar behaviour when investigating the effect of recycling SS316L powder through multiple sieving procedures. They found that reusing powder for multiple builds, in the order of up to 30 recycles, with intermittent rejuvenation does not seem to notably affect powder characteristics or the quality of the manufactured parts. While there was some indication of a gradual rise in oxygen and nitrogen levels, this does not appear to exert a significant impact on the PBF-LB/M processed parts. Therefore, employing sieving after each build cycle was shown to be an effective method for re-conditioning the powder. Delacroix et al. [21] reported similar results, after recycling SS316L powder for up to 15 cycles. They found that recycled powders exhibit a slight increase in particle size, even after sieving with a 50 μm mesh, and irregularly shaped particles can persist in the feedstock. This can enable an improved flowability in recycled powders, which the authors primarily attributed to an increased presence of particles with surface oxidation (oxygen increase of 475–675 ppm). Other chemical changes found by Delacroix et al. included the presence of partially oxidised spatter particles in recycled powders after sieving, with Mn and Si-rich oxide nodules particularly found [21]. Delacroix et al. attributed their presence as potentially originating from vapor-entrained particles that may have oxidised whilst in flight. Another significant change was the increase in the amount of ferrite (4 wt%) in 15-times recycled powder, despite the virgin powder being almost fully austenitic. Ferrite particles are typically magnetic and can lead to clustering both in the powder and the final PBF-LB/M manufacture component, whilst also offering a single crystal morphology as they solidify under supercooling conditions. Therefore, the importance of introducing a suitable sieving process is crucial for reducing powder degradation, large powder agglomerates and the presence of magnetic powder particles. Delacroix et al. [21] also reported that the final microstructure of SS316L samples with increasing numbers of powder recycles saw a refinement in grain size, possibly arising from oxide inclusions contributing to the pinning of grain boundaries.

Despite such changes to the powder characteristics and microstructures of PBF-LB/M samples, Delacroix et al. [21] reported no significant differences in microhardness and tensile properties with powder recycling, indicating that SS316L powder can be used up to 15 times in the PBF-LB/M process without compromising the mechanical properties of elaborated specimens. This was also the case for Douglas et al. [17], who found that the tensile behaviour of SS316L shows little change with powder recycling, and any reductions in ultimate tensile strength (UTS) and yield stress (YS) were often small or insignificant.

Although these previous studies have extensively investigated the effects of powder recycling on mechanical performance, an understanding on how such changes influence the cyclic and corrosion properties of PBF-LB/M manufactured samples containing recycled powder is less well understood. A major benefit for understanding this would be the ability to reduce testing on reference samples for builds using recycled powder. Currently, substantial amounts of testing is needed on reference samples for each build to monitor any potential changes to part properties. If the recycling of powder was better understood, then this could be scaled back to reduce the number or variety of tests, resulting in lower lead times and a cost saving on manufacture and testing.

This paper will investigate how the powder feedstock of SS316L evolves through the PBF-LB/M production route and how this may affect the final properties of PBF-LB/M components. This can then be used to enhance the understanding of how recycling affects end components, whether there is a recycling limit for powder and how best to monitor the powder evolution. This study involves a thorough characterisation of the powder particles after different levels of recycling and

understanding how several factors such as powder size distribution (PSD), flowability, chemistry and morphology change through their life cycle. This will subsequently be followed by analysing how such changes affect the PBF-LB/M material after two alternative post-processing treatments; namely a stress relieving heat treatment (SRHT) and a HIP procedure, designed to reduce any process-induced defects such as porosity. This will include analysing the respective microstructures, crystallographic texture, chemistry and defect populations and how these features influence the resulting pitting potential, low cycle fatigue (LCF) properties and tensile and impact strengths.

2. Experimental methods

2.1. Material

In this research, PBF-LB/M SS316L specimens were manufactured from powder feedstock after various stages of recycling to understand the effects of recycling on the resulting mechanical properties. The virgin powder was supplied from LSN Diffusion and created by gas atomisation, with no reused powder present. The chemistry of the virgin powder is displayed in Table 1, and the powder size distribution (PSD) of the virgin powder is given in Table 2. Both sets of data were supplied by LSN Diffusion.

During the PBF-LB/M process, a given virgin powder batch is typically in the order of one tonne in mass. This batch is then typically allocated a batch number which follows with the powder until it is fully consumed. However, the one tonne of bulk powder within a powder lot is too large to be fully loaded in to a PBF-LB/M machine for a single build run. Therefore, powder is drawn from the batch associated with the machine and topped up with virgin powder as and when is necessary. In addition to the refilling of the machine from the new powder batch, powder that is not used in the part production is also collected and reused in subsequent builds. This is described as reused powder. Therefore, for subsequent builds after the first manufacture run, the powder used may be 100 % recycled powder from the previous build, or a mixture of recycled powder and virgin powder from the powder batch. In addition to this, recycled powder may have been reused once or multiple times and therefore tracking the true condition of a selected batch of powder is extremely difficult.

Before powder is loaded into the PBF-LB/M machine between builds, it is sieved to remove particles greater than 63 μm in diameter. After this, powder is mixed within a sealed drum before being loaded back in to the machine. The purpose of this procedure is to avoid segregation of the powder particles by size. It also allows for the proper mixing of any new virgin material added to the powder feedstock. A reference powder sample of 150 g is also taken from the mixed powder drum. This is collected using a powder thief to collect 25 g samples at 6 different locations to create a final mixed sample of approximately 150 g. In this study, powder has been collected for analysis after 2 sieves (predominantly virgin powder), 15 sieves (mid-level of recycling) and 30 sieves (high-level of recycling).

Table 1
Nominal chemistry of virgin SS316L powder for PBF-LB/M.

Element	wt%	Element	wt%
Al	0.005	N	0.005
B	0.001	Nb	<0.010
C	0.010	Ni	12.420
Co	0.020	O	0.010
Co + Ta	0.020	Ph	-
Cr	17.040	S	0.014
Cu	0.010	Si	0.350
Fe	Balance	Ti	<0.005
Mn	1.200	V	<0.010
Mo	2.530		

Table 2
Powder size distribution (PSD) of virgin SS316L powder for PBF-LB/M.

D_x Number	Particle Size Diameter (μm)
D_1	10–16
D_4	12–18
D_{25}	20–26
D_{50}	26–32
D_{75}	34–40
D_{90}	43–49

2.2. Powder analysis

A series of methods were employed to characterise the three different powder conditions in order to understand the flowability, chemistry, morphology and particle size distribution.

2.2.1. Scanning electron microscopy (SEM), electron back-scatter diffraction (EBSD) and energy dispersive X-ray spectroscopy (EDS)

Particle size distribution (PSD) analysis was completed with the use of scanning electron microscopy (SEM) and subsequent image analysis. For this, powder samples were mounted on to conductive carbon sticky tape and attached to 12.7 mm diameter circular pin stubs. These were then blown with compressed air to remove any loose powder particles. Samples were loaded in to a JEOL JSM 7800 F (FE-SEM), fitted with a tungsten source. For PSD analysis, a BSE image was taken with an accelerating voltage of 15 keV.

Oxford Instruments AZtecAM software was used to analyse the PSD of the powder. Once a BSE image had been generated, a median filter was applied as well as a separation filter to threshold the image. A stitched rectangular scan area of around 30 mm^2 made up of 192 individual scans at a magnification of 250x and 9 mm working distance was analysed. Each stitched image contained a minimum of 20,000 features. Features under 2 μm in size were filtered out as noise.

For general imaging using the JEOL, images were taken using the secondary electron detector. Accelerating voltage, aperture size, spot size, beam current and working distance were varied according to requirement. The JEOL was equipped with an Oxford Instruments X-Max N detector, which was used for EDS chemical analysis. Maps were completed on individual powder particles to identify the composition of oxides on the powder surface. For EDS, the accelerating voltage was set to 20 keV to generate a sufficient number of secondary electron emissions to accurately identify elements.

EDS and EBSD analysis were also performed on powder and consolidated samples using the Hitachi SU3500 system. To enable this, the Hitachi SU3500 was fitted with an Oxford-HKL Nordlys II detector. Samples were polished with 0.1 μm OPS solution on a vibratory polisher for 2 hours before EBSD scans. Analysis of EDS and EBSD data was completed using AZtec software from Oxford Instruments. For EBSD analysis, a step size of 0.25 μm was adopted to define the differences within the fine PBF-LB/M microstructure. Samples were mounted at 70 ° in the SEM chamber and scans were completed at magnifications between 300–500x with a working distance of approximately 20 mm. To accurately determine the difference between similar FCC and BCC unit cells, scanning speed was sacrificed for greater accuracy. Scan setup parameters included 2×2 sample binning, and a minimum of 12 Kikuchi bands analysed per crystal system.

EBSD post processing and analysis was completed on HKL Channel 5 software from Oxford Instruments. This generated phase maps, inverse pole figures (IPF), recrystallisation maps and misorientation maps which can be used to indicate residual stress. The minimum angle of misorientation to differentiate grain boundaries on maps was set at 1.5 °. Lower misorientation angles were considered but they were below the precision of the data generated. From this, grain size measurements were generated for the different samples.

2.2.2. Laser diffraction

A Malvern Mastersizer 3000 was also used for laser diffraction to calculate the powder size distribution. The machine uses the scattering of light around particles to identify their size. For this setup, the particle type was selected as spherical. The material was selected as stainless steel with a refractive index of 2.757. Distilled water was used as a dispersant with a refractive index of 1.33. The machine was washed out three times with fresh water and ultrasonic cleaning was performed between tests on powder to avoid contamination.

A powder sample approximately 2 g in weight was dispersed in water and mixed by the machine. The exact amount of powder was the suitable amount to satisfy the obscurence limits of the machine, which were set not to exceed 20 % for a balance between signal and accuracy. Once the powder slurry had been thoroughly mixed, it was passed across a laser light source and the level of diffraction was used to calculate powder size.

2.2.3. Inert gas fusion

Inert gas fusion was completed by Carpenter Additive in an accredited laboratory conforming to ISO 17025 [22]. This method is capable of avoiding the presence of surface oxides and as such, providing a more suitable representation of the oxygen and nitrogen content of the bulk powder chemistry. Approximately 10 g of powder was provided per sample, although not all of this was necessarily consumed.

2.3. Laser powder bed fusion

In this research, a series of three base plates containing 22 horizontally (0°) orientated octagonal rods, of 21.5 mm in width and 105 mm in length, were manufactured, each of which employed powder after different levels of recycling (namely 2, 15 and 30 sieves). All rods from the three baseplates (as depicted in Fig. 1) were manufactured in an EOS M290 machine in a nitrogen atmosphere using the standard manufacturer recommended process conditions for SS316L, with a layer thickness of 20 μm and a volumetric energy density (E_v) of 100 J/mm^3, as defined by the equation given in Eq. 1:

$$E_v = \frac{P}{v \bullet h \bullet t} \quad (1)$$

Where P represents the laser power (W), v is the scanning velocity (mm/s), h is the hatch spacing (mm) between adjacent scan passes and t is the layer thickness (mm).

Once each of the three respective base plates were constructed, they were each split into two to create two sets of 11 rods. One half of the rods were hot isostatically pressed (HIP) whilst the other half were stress relief heat-treated (SRHT) so they could be safely removed from the base plate while remaining as close to the as-built condition as possible. The HIP cycle consisted of a heat treatment above the SS316L solution temperature (1000 °C) and was held at this temperature for 2–3 hours prior to cooling, at a pressure between 130 and 170 MPa. The exact parameters of the HIP procedure, including the ramp rates, are commercially sensitive. The SRHT cycle consisted of rapid heating to 700° C, holding for 2 hours, followed by furnace cooling down to room temperature. Once each of the rods were removed from their respective base plates via wire EDM, they were then machined into a variety of test piece geometries for tensile, low cycle fatigue and Charpy impact experiments.

2.4. Test methods

2.4.1. Low cycle fatigue testing

Low cycle fatigue (LCF) experiments were performed using a servo-hydraulic mechanical test machine under strain controlled conditions, in accordance to ASTM E606 [23]. Each test was carried out using a 0.004 s^{-1} triangular waveform and a fully reversed R value of −1, in a controlled laboratory environment of 21 °C. To provide a range of strain-life data, several applied strain amplitudes (ε_a) were employed. The number of fatigue cycles to failure (N_f) is reported as a 25 % drop from the peak load at the half-life, stabilised condition (as determined through linear regression). All samples were tested until failure, or once 100,000 fatigue cycles were surpassed, upon which the test was stopped, the sample was unloaded, and the test was deemed a run-out. The specimen dimensions for the test-pieces is presented in Fig. 2. All samples were finished with a longitudinal polish according to ASTM E606 [23].

2.4.2. Tensile testing

Uniaxial tensile specimens were manufactured in accordance to ASTM E8–04 [24], with the dimensions depicted in Fig. 3a). All specimens were finished with a longitudinal polish and a 0.3 μm surface finish. The tensile tests were performed on a Dartec 100 kN electric screw test machine, with Dartec 9610 control system and Dartec Workshop 96 software. For all tensile tests, a constant strain rate of

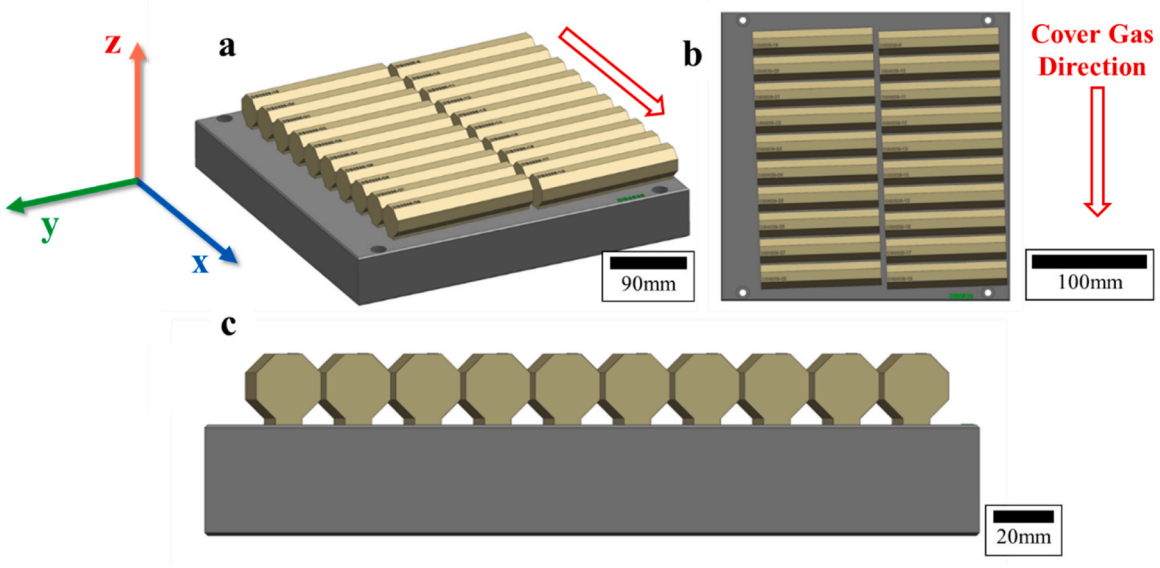

Fig. 1. The build plate design containing the octahedral rods a) Isometric view b) Plan view c) Side view.

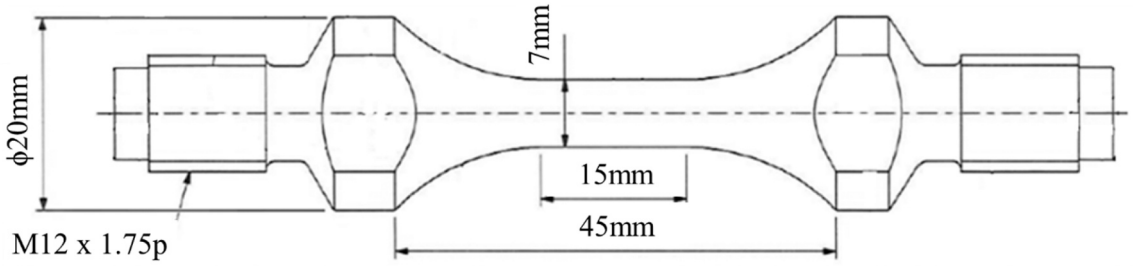

Fig. 2. Sample geometry for low cycle fatigue testing.

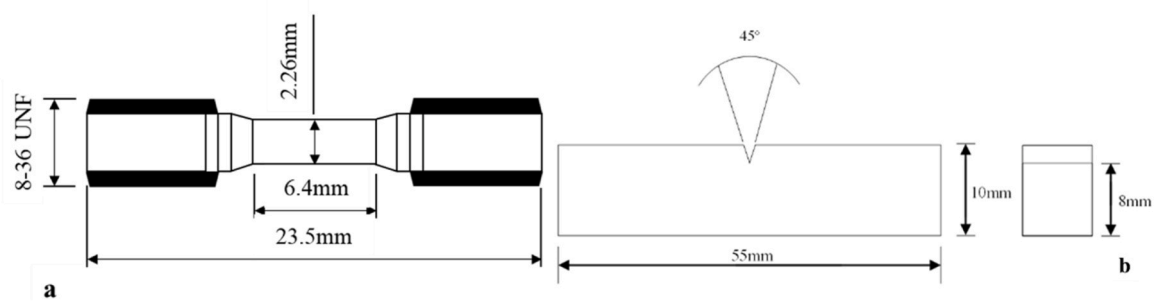

Fig. 3. Test piece geometry for a) Uniaxial tensile b) Charpy impact experiments.

0.005 mm•min^{-1} was used until the yield strength was exceeded, upon which the 12 mm extensometer was removed and a second strain rate of 0.05 mm•min^{-1} was employed until failure. The purpose of this was to protect the extensometer from over exertion at high strains. All test procedures adhered to ASTM E8–04 [24], with 25 data points recorded per second and strain measured through extensometry. All tests were performed in a controlled laboratory temperature of 21 °C. Yield strength was determined by the offset method defined in ASTM E8–04, and elongation was determined after fracture according to the same standard [24].

2.4.3. Charpy impact testing

Charpy impact tests were performed on an Instron MPX testing machine. Samples were manufactured to the ASTM E23 [25] standard geometry of 10 mm×10 mm x 55 mm with a 2 mm notch at a 45 ° angle (as depicted in Fig. 3b)). For consistency, the specimens were machined so that the notch was aligned with the top of the octagonal rod in each instance. Three samples were tested per condition and an initial test with no sample was completed beforehand, from which the value of energy absorbed (if any) was removed from the subsequent test results. All tests were performed in a controlled laboratory temperature of 21 °C.

2.4.4. Cyclic polarisation

A Gamry 1010E potentiostat was used to complete open circuit and cyclic polarisation testing of a selection of PBF-LB/M SS316L samples containing different levels of recycled powder. Cyclic polarisation involves putting a potential through a sample to promote corrosion and then reversing this potential to promote re-passivation. From this, a pitting potential and re-passivation potential can be determined. These equate to the point at which the oxide layer is breached, and the subsequent point at which it heals. The open circuit potential for corrosion can also be decerned which is the standard potential of the sample within the media, which in this case is salt water.

Samples were mounted in a circular sample holder which acted as the working electrode in a three-electrode arrangement. A 0.78 cm^2 surface area of the sample was exposed. The reference electrode was a saturated calomel electrode and a platinum plated electrode was used as a counter. The reference electrode was positioned close to the working electrode and all three electrodes were submerged in 3.5 % salt solution. Cyclic polarisation scans were then recorded with a forward scan speed of 0.16 mV/s at a start point of 0.2 V below the open circuit potential. This was reversed when a current density of 10 mA/cm^2 was reached and stopped when the voltage reached the original starting value.

2.5. Microscopy, defect and fractographic analysis

A Hitachi SU3500 SEM, with electron backscatter diffraction (EBSD) capability, was used to inspect the microstructures and the fracture surfaces of the different sample types. For EBSD analysis, scans were acquired using a step size of 1.5 μm and 4 ×4 binning. The phases chosen for acquisition were FCC-Fe and BCC-Fe, with the band detection mode optimised for EBSD. EBSD data was analysed using the Tango plug-in included in the Channel 5 software. Grain detection was performed using the grain area determination in Tango software, where no border or corner grains were included in the analysis. Grain size of the XY and XZ faces of each sample type was measured by Channel 5 software.

A Zeiss Smartzoom 5 optical microscope was used to analyse the defect population of a selection of the different LPBF SS316L variants. Samples were prepared using standard metallographic procedures, and were then subjected to vibratory polishing on a VibroMet 2 polisher with OP-S (colloidal silica suspension) for ~8 hours to remove any remaining minor deformations.

Samples for porosity measurements were imaged at 100x magnification. Three images were taken per sample with no overlap between the images, in both the XY and XZ orientations. Porosity was identified in images using thresholding and the analyse particles function on ImageJ. Any pores with an area under 2 μm^2 were removed from the results to eliminate noise. Thresholding of images to identify porosity was adjusted manually for every image for greater accuracy.

3. Results & discussion

3.1. Powder analysis

As discussed earlier, previous studies have shown a slight increase in the PSD of SS316L with powder recycling [26,27]. This is primarily due

to fine particles being preferentially consumed during manufacture and their consumption in to larger particles through spatter and satellite particles. PSD has been characterised previously using both image [27] and laser diffraction based methods [28].

As shown in Fig. 4a), through laser diffraction, the PSD curves for the start, mid and end point (virgin, mid- and most recycled powder) of the powder particles have shown a coarsening over the lifecycle, with the D_x numbers provided in Table 3. The powder sample at 2 sieves had already undergone one build through the machine as sieving and sampling occurs before building. In between then and 15 sieves, when the next powder sample was taken, significant amounts of virgin powder were added, as follows: 131 kg at 4 sieves, 75 kg at 5 sieves, 15 kg at 7 sieves, 70 kg at 10 sieves, 28 kg at 11 sieves and 30 kg at 12 sieves. Although there is not enough evidence to suggest a full stabilisation of the PSD with powder recycling once the batch is coarse enough, laser diffraction has shown that the PSD can be reset to some degree by the addition of virgin powder. The addition of virgin powder to top up the powder batch only occurs if there is virgin powder available so the effect is limited to earlier powder samples. However, controlling the initial PSD means the final PSD can be regulated as powder will only coarsen so far before it is fully consumed.

In addition to PSD analysis from laser diffraction, PSD measurements were recorded by SEM image analysis using AztecAM software, as displayed in Fig. 4b). Similarly to the laser diffraction analysis, the PSD curves for the samples from 2 and 15 sieves show very little variation and the 30 sieves sample has a coarser PSD. However, the variation between the 15 and 30 sieves samples is more significant than that derived from laser diffraction. The 30 sieves peak has collapsed and the tail of the curve has shifted significantly. This collapse in the peak with recycling has previously been shown by Heiden et al. when they measured PSD using SEM analysis [26].

In each of the respective plots, the PSD curves start from 10 μm due to the filtering out of all data less than this value. This is due to the difficultly of filtering and thresholding of fine particles using image analysis. This does not mean that these fine particles do not exist in the powder but both techniques appear to struggle with the identification of particles below 10 μm. Images from the SEM proves that these small particles (under 10 μm) are indeed present, as shown in Fig. 5, which shows the thresholding of the powder after 2 sieves. In this figure, particle *a* refers to a correctly identified particle with a diameter below 10 μm that would have typically been filtered out during analysis. Particle *b* is a sub 10 μm diameter satellite particle with is incorrectly identified as an individual particle. Both examples show that these sub 10 μm particles exist, but that their quantification is difficult to achieve. The number of particles filtered out was 28 % for 2 sieves and approximately 20 % for 15 and 30 sieves, suggesting that more fine particles may have existed in the 2 sieves samples.

Comparing the D_x numbers of the two analysis techniques (Table 3), both laser diffraction and SEM analysis show minimal variation between the 2 and 15 sieves powder but subsequent coarsening of the most reused powder. Both are therefore in agreement regarding the trends in the PSD.

Table 3
D_x numbers for the powder batch after 2, 15 and 30 sieves as determined by laser diffraction and SEM with AztecAM software.

Sieve Count	D numbers (laser diffraction)			D numbers (AZtecAM)		
	D_{10} (μm)	D_{50} (μm)	D_{90} (μm)	D_{10} (μm)	D_{50} (μm)	D_{90} (μm)
2	20	32	51	14	23	39
15	20	32	54	12	21	36
30	24	36	57	15	32	50
Overall Difference (2–30 sieves)	+4	+4	+6	+1	+9	+11

Image analysis through AztecAM was shown to provide a finer PSD curve with lower particle sizes across all D_x numbers. In addition, the coarsening observed is greater in the D_{50} and D_{90} size but not the D_{10} as fine particles were filtered out. As such, the bottom end of the PSD is not as accurate. Overall, SEM analysis was more sensitive to changes in the PSD but also less reliable as there are more areas for significant error from AZtecAM. Variations to the image contrast, overlapping powder from sample preparation and errors from thresholding powder particles can all lead to large deviations. The advantage of image analysis is that it can identify fine particles that are missed by other techniques and demonstrates greater variation in results.

To test the flowability of metallic powder, Hall Flow tests were completed to ASTM B213–20 [29]. 50 g of metallic powder was weighed out beforehand which was subsequently poured in to the Hall flow funnel with the funnel orifice sealed. The funnel was placed at approximately 50 mm above a receptacle dish, from which the funnel orifice was unsealed and at the same time a stopwatch was started. As soon as the last powder had left the funnel the stopwatch was stopped and the time was recorded. The tests were completed three times per powder sample and repeated if powder flow became interrupted during the test. In this study, the powder showed a small increase in flowability of approximately 10 %, from 20 s for 2 sieves powder to 18 s for the most recycled 30 sieves powder. Previously, Mellin et al. [30] found that a relationship exists of increased flowability with powder reuse when analysed using Hall Flow. Yet, investigations in to the effects of powder reuse on powder flowability for PBF-LB/M have often been conflicting or inconclusive. The most prevalent relationship appears to be one of powder coarsening due to powder reuse that leads to fewer fine particles and less powder agglomeration. This in turn leads to an increase in flowability. Yet, the observed increase in flowability after recycling in this study is hindered by the regular introduction of new virgin powder that exhibits a finer particle size, and hence, a reduced flowability.

From the inert gas fusion experiments, both the oxygen and nitrogen

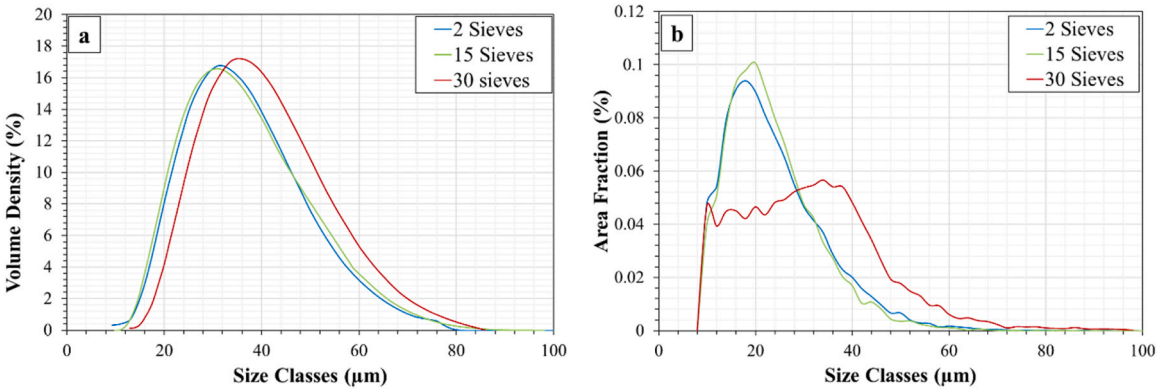

Fig. 4. The PSD curves for powder after 2, 15 and 30 sieves of recycling, as determined by a) laser diffraction and b) SEM with AztecAM software.

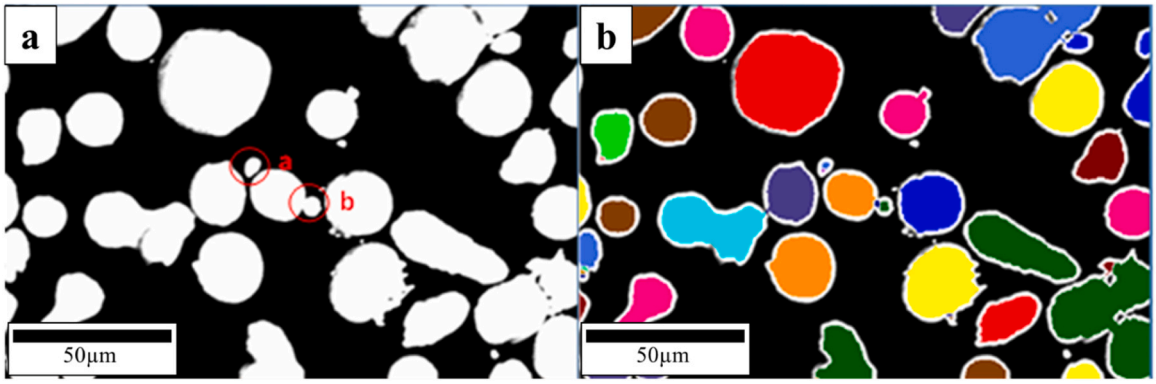

Fig. 5. a) BSD image of 2 sieves powder showing fine satellite and segregated particles. Powder particle a and b have maximum lengths of 6.7 and 6.5 μm respectively, b) 2 sieves powder post thresholding by AZtecAM.

content of the powder were seen to increase with powder recycling level, as presented in Fig. 6. Oxygen content increased from 442 ppm to 487 ppm, representing a 10 % increase. Over the same level of powder recycling, the nitrogen content increases from 677 ppm to 694 ppm, a 2.5 % increase. This occurs despite the build chamber being backfilled with nitrogen, where the pickup associated from this remained low. In previous studies, Murray et al. [20] observed a larger increase in oxygen content in the order of 20 % when recycling from 1 to 30 builds, whilst Delacroix et al. [31] also found significantly higher levels of oxygen with recycling. It is difficult to determine the precise reasons for the differences in oxygen pick-up across the different studies, but particular factors such as the adopted process parameters or the thickness of the oxide scale on the surface of unmelted powder particles could be considered. In the study by Murray et al., they used a maximum E_v value of 90 J/mm^3 [20], whilst Delacroix et al. used 116 J/mm^3 [31], as opposed to 100 J/mm^3 used in the current study. Likewise, the extent of oxidation is promoted by the elevated temperatures and adequate oxygen partial pressure during the manufacturing process. Galicki et al. [32] reported that spatter particles containing elevated levels of oxygen and their subsequent re-introduction into the powder bed process are unlikely to be a significant source of oxygen pick-up, but such a factor could also be considered. Furthermore, Cr is typically added to SS316L to improve oxidation resistance, but interestingly the Cr wt% had minimal variation across the different studies. The SS316L powder used by Delacroix et al. contained 17.5 wt%, Murray et al. contained 16–18 wt% and the current study had 17.04 wt% Cr [20,31]. As such, given that the Cr content was relatively consistent across the three studies, it is not considered to be a significant factor influencing the differing oxygen pick-up behaviours.

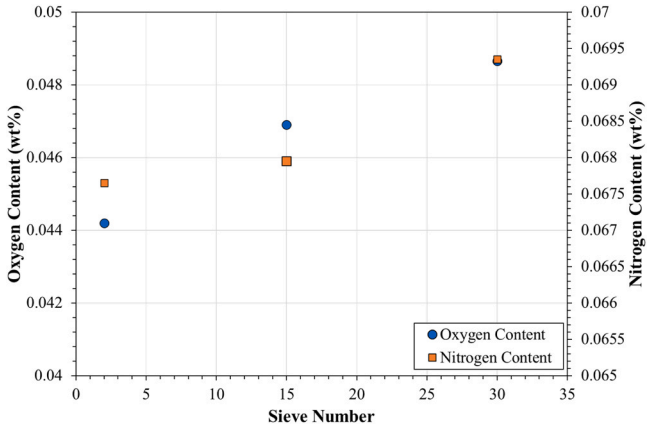

Fig. 6. Bulk oxygen and nitrogen content in powder samples at different levels of recycling.

Energy Dispersive X-ray Spectroscopy (EDS) was used to characterise the composition of oxides that formed on recycled powder particles. Examples of this are shown by a powder particle with melted satellite particle scale (Fig. 7a)) and of a remelted spatter particle (Fig. 7b)) after 30 sieves. Both EDS maps show that the oxides that formed on the surface of powder particles are lean in iron and rich in oxygen, manganese and silicon. Manganese and silicon rich oxides have previously been identified on recycled/spatter particles in SS316L powder [33,34]. By studying the oxide stability and the partial pressure of oxides formed, Lu et al. ranked common oxidising elements within SS316L as the following: Si>Mn>Fe>Ni [33]. The lower partial pressure of oxygen for Si and Mn oxides encouraged their formation. For other oxides to form, they require a higher partial pressure of oxygen which is limited within the build chamber. This suggests that with future enhancements to PBF-LB/M processing, better backfilling and removal of oxygen may contribute to fewer and a less variety of oxides.

Characterisation of these oxides to determine their exact composition has shown them to be a mix of species. Lu et al. speculated that in addition to SiO_2 and MnO, differing quantities of these elements may react to form $MnSiO_3$ or $Mn2SiO_4$ [33]. This was shown to be true by Gorji et al. through synchrotron analysis where $MnSiO_3$ was observed to increase in quantity in recycled SS316L powder [11], whilst in their study, Heiden et al. identified both SiO_2 and $MnCr_2O_4$ oxides on the surface of recycled SS316L powder [26]. Formation and detection of such oxides is important to understand as they have been shown to affect the melting and solidification of powder in PBF-LB/M and promote a greater number of oxide inclusions within the final fused material [35]. Oxide inclusions that are rich in Mn and Si have been associated with a reduced performance for AM 316 L material in impact experiments and for stress corrosion cracking [36]. The SEM imagery and inert gas fusion measurements have indicated that the number of oxides increases with powder recycling. Likewise, EDS scans have shown oxygen residing in the form of oxides on the surface of the powder particles.

In addition to oxygen, previous studies of powder recycling in SS316L have shown an increase in the ferrite content of powder with recycling [26,37,38]. Ferritic powder is magnetic, whereas austenitic powder is not, which makes it more susceptible to agglomeration of powder particles that could lead to clumping of powder on the build plate or poor flow properties in the powder. EBSD stich maps (Fig. 8) were recorded in order to scan a large enough sample of powder. IPF maps were also generated as part of this process. As the orientation of powder is random, the directions of texture generated are redundant. However, these maps do reveal that all ferritic powder particles have a single crystal microstructure. This is due to rapid cooling of powder ejected from the laser. Heiden et al. established that these particles had no noticeable change in composition that could affect phase composition but that instead these particles are formed as a result of spatter that had undergone large thermal gradients [26]. As ferritic powder is formed via

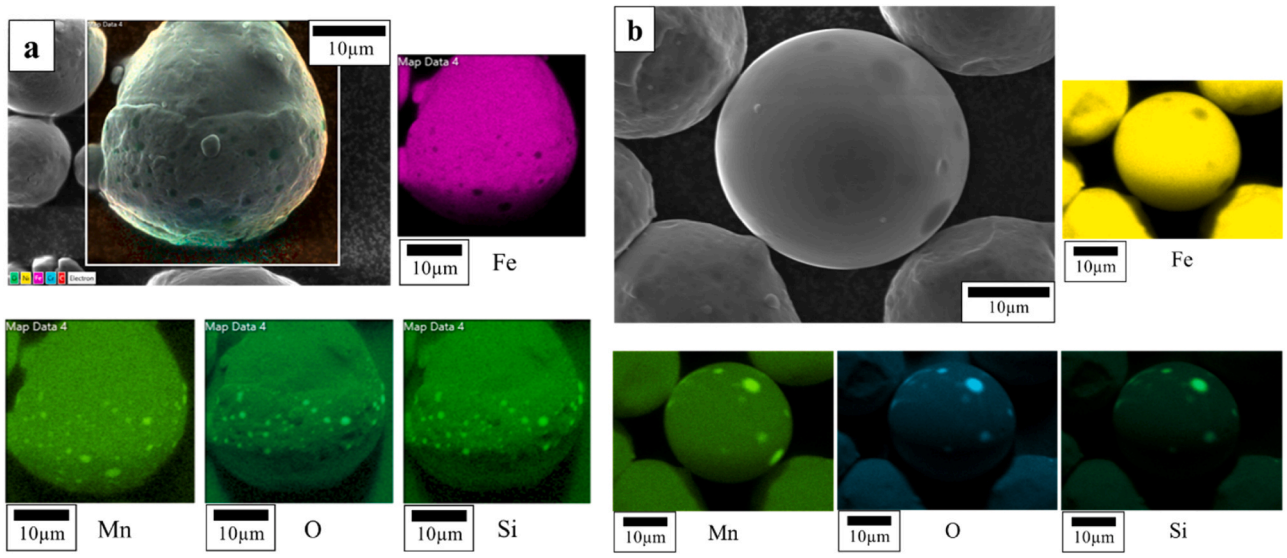

Fig. 7. EDS maps of a) a powder particle with melted powder on its lower half, potentially from a satellite powder particle and b) a smooth surfaced spatter powder particle. Oxides on the surface are rich in manganese, silicon and oxygen while being lean in iron. Both EDS maps are taken on 30 sieves recycled powder.

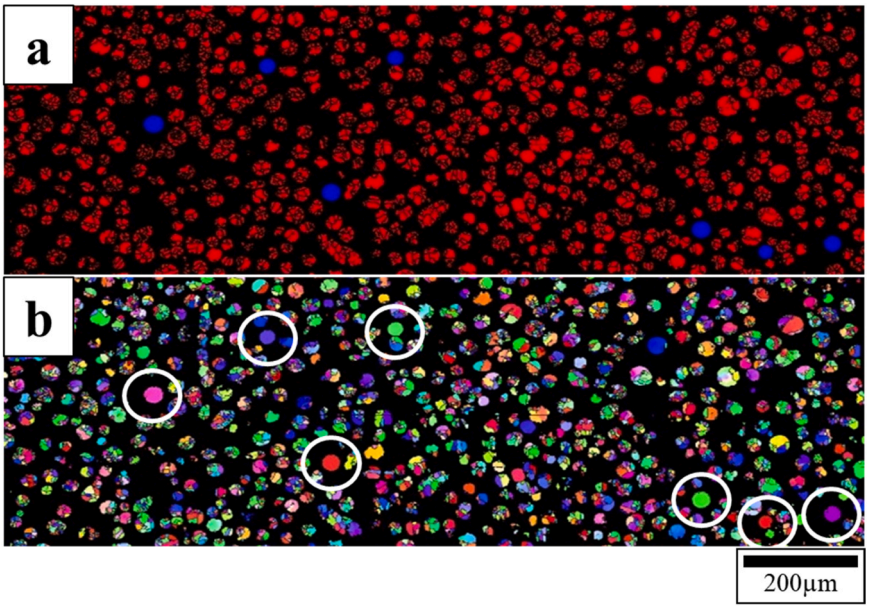

Fig. 8. EBSD stitch maps of 30 sieves powder, a) phase map displaying austenite (denoted by red particles) and ferrite (blue particles), b) IPF map of powder showing single crystal powder particles occur when powder is ferritic, these particles are circled in white.

spatter, the increase in ferrite content from 0.8 % to 1.4 %, as displayed in Table 4, also indicates the increase in spatter particles within the sample. However, despite this marginal increase, the low levels of ferrite seen in the heavily recycled material is still favourable for corrosion resistance, given that in previous research, ferrite content was found to reach 6 % by volume in recycled SS316L [38]. In the study by Pinto et al. [38], a far lower E_v value of 22 J/mm^3 was utilised. Therefore, it is likely that the material experienced high cooling rates in the build chamber and the retained ferritic particles were unable to transform to austenite. At this point, defects can occur due to clumping of the magnetic powder, however, after 30 sieves the powder in this study has not reached this level where it would be considered to be a concern (<2.2 %). The single crystal nature of the ferritic powder confirm it was formed via rapid cooling and most likely as a result of recoil spatter [26]. Different processes will have varying laser parameters and gas flow, which will in turn increase or reduce the amount of recoil spatter that generates ferritic powder and determine how much is removed. The larger sample size of approximately 1000 powder particles that were studied provides confidence that the levels of ferrite powder observed are accurate to the overall sample.

Table 4
Ferrite content of powder from samples taken at the start and end stages of powder recycling as determined by area fraction from EBSD.

Recycling Level	Powder Particles Analysed	Ferrite Content by Particle Frequency (%)	Ferrite Content by Area (%)
2	975	0.82	1.54
30	1057	1.42 %	2.16

3.2. Laser powder bed fused (PBF-LB/M) samples

3.2.1. Material

3.2.1.1. Microstructure. EBSD maps were collected to characterise the microstructure of a selection of SRHT and HIP samples at different powder recycling levels, both parallel (XZ) and perpendicular (XY) to the build direction. Some commonalities are present across all samples. Firstly, the phase composition of all samples was near 100 % austenitic in all cases (Fig. 9). An increase in ferrite content associated with the raw powder feedstock did not translate into an increase of ferrite in the bulk material. This could be due to the laser power during PBF-LB/M, where the powder within the melt pool is likely fully consumed and therefore any remaining ferritic microstructure can be resolidified as austenitic.

Also true across all samples was the presence of <101> texture parallel to the build direction and an anisotropic microstructure where the grains were elongated in the XZ plane (Fig. 10). Due to the directional cooling of PBF-LB/M material towards the build plate, grains experience epitaxial growth in the build direction which creates an anisotropic microstructure [39]. In addition to this, the high energy density used for the manufacture of PBF-LB/M SS316L samples also promotes this directional cooling and in turn the <101> texture [4]. The average texture (otherwise known as maximum multiples of uniform density (MUD)) values decreased however for the SRHT samples, from 7.2 in the 2 sieves sample to 4.2 in the 30 sieves sample. Yet in the HIP samples, the MUD value raised slightly, from 2.9 to 4.0, as given in Table 5. This indicates that the HIP procedure is promoting grain growth with increased texture after recycling.

In addition to the changes to crystallographic texture, aspect ratios were also calculated to provide a quantitative representation of potential anisotropy for each respective plane. This was achieved using the mean linear intercept method, and then dividing the length of the minor axis by the length of the major axis of a given grain. For SRHT samples, the aspect ratio ranged from 0.51 to 0.52 in the XY plane (Fig. 11) and 0.34–0.36 in the XZ plane, indicating more equiaxed grains in the XY than the XZ, as typically expected for AM material. For HIP samples, the XY aspect ratio is similar to that of SRHT samples, approximately 0.51–0.53, but for the XZ orientation it is slightly higher than the SRHT condition samples at 0.39–0.42. This suggests partial recrystallisation of the microstructure during HIP where new grains are more isotropic and are less textured. Furthermore, the average grain size of HIP samples tends to larger sizes than equivalent SRHT samples. Average grain size in the XY orientation are 31 % larger in the XY plane and 47 % greater in the XZ plane for HIP samples, compared to the SRHT equivalents. Grain size did vary slightly between samples manufactured at different levels of powder recycling, however a trend relating grain size with powder recycling is non-existent. It should be noted that EBSD scans are limited in scan area and therefore some variation is expected in the results, particularly for grain size. Despite differences of up to 40 μm^2 between samples in the XZ plane, this is likely due to the limited scan area of the map.

3.2.1.2. Porosity. From the investigation of studying the presence of defects in the different PBF-LB/M SS316L samples, porosity was found to slightly increase from a volume fraction of 0.01 % to a high of 0.08 %, as powder recycling increased from 2 sieves to 30 sieves in the SRHT material (as shown in Table 6). The increase in total porosity with increasing powder recycling may be due to the reduction of fine particles with increased recycling. Fine particle proportion is closely related to build plate packing, as these particles can occupy smaller vacancies within the build plate, improving build plate packing and subsequent mechanical performance [15]. This minor increase in porosity has also been observed within other studies on recycled powder [21,40]. As well as porosity increasing, pore size was also greatest in the 30 sieves SRHT samples in both the XY and XZ plane. Yet, despite this variation, it is important to note that the overall porosity in all samples remains relatively small and that all samples, in both the SRHT and HIP conditions, were above 99.9 % dense. This is in line with previous studies that

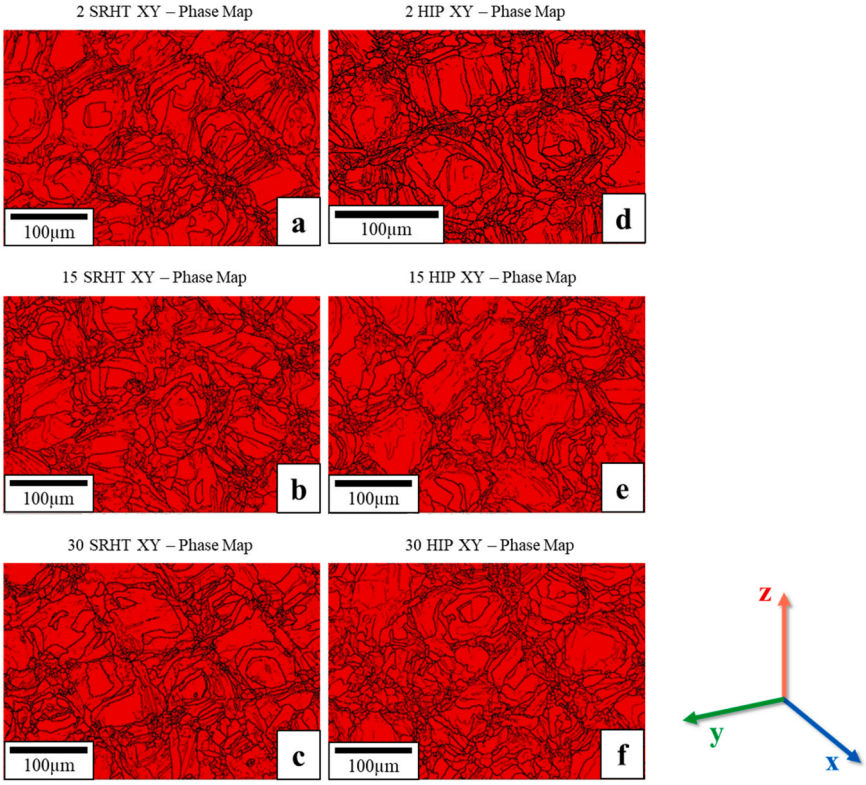

Fig. 9. Phase maps of SRHT and HIP samples at all levels of powder recycling in the XY orientation. Red colour indicates the austenite phase, blue colour represents the ferrite phase.

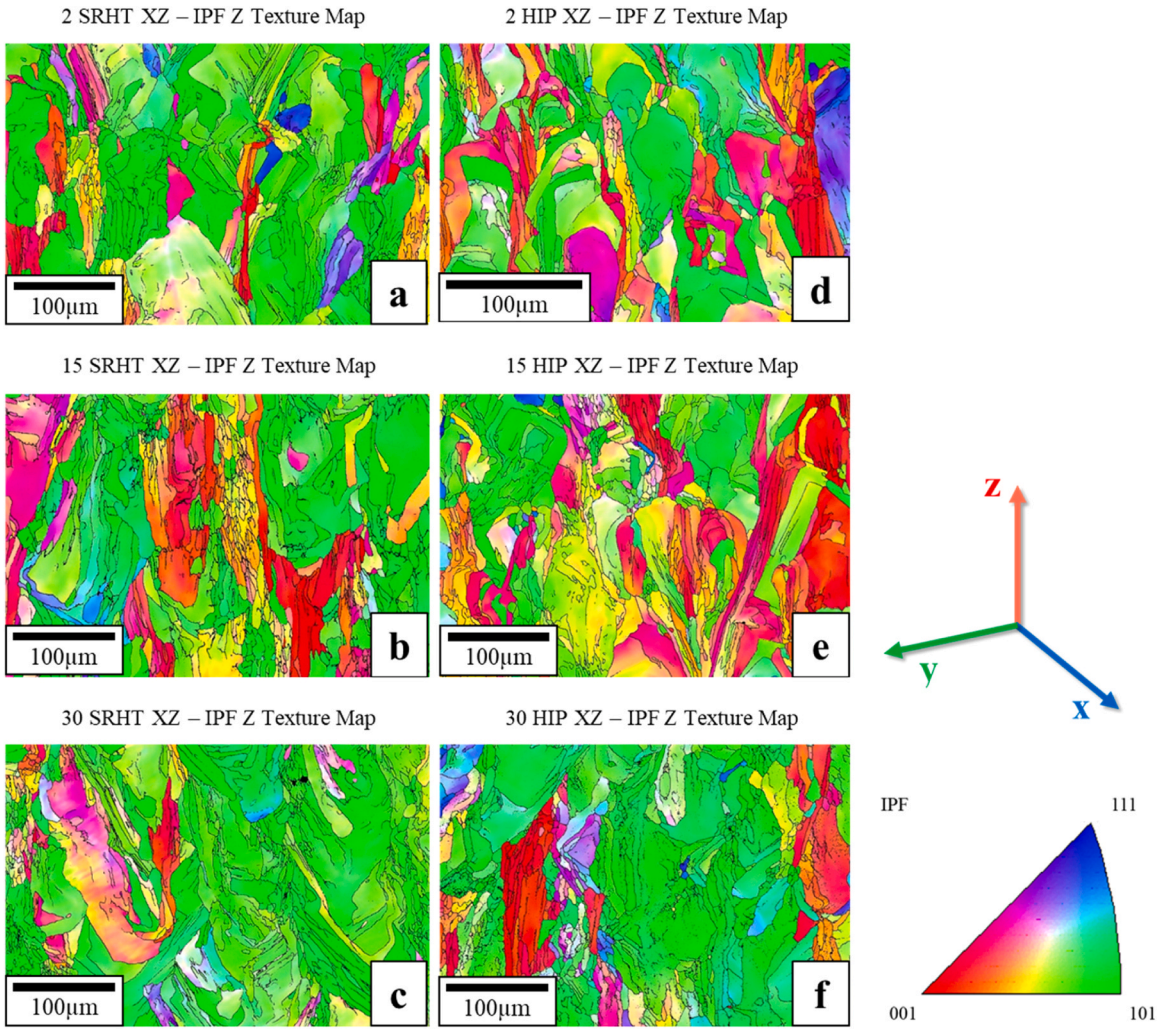

Fig. 10. Inverse pole figure maps, orientated in the Z direction parallel to the build direction, of HT and HIP samples at all levels of powder recycling in the XZ orientation showing elongated columnar grains parallel to the build direction.

Table 5
Microstructural measurements for all PBF-LB/M samples as calculated through EBSD.

Sieve Count	SRHT/ HIP	Orientation	Average Grain Size (µm^2)	Aspect Ratio	Maximum <101> MUD value
2	SRHT	XY	109.4	0.51	7.61
2	SRHT	XZ	159.9	0.36	6.78
2	HIP	XY	125.4	0.53	2.44
2	HIP	XZ	263.6	0.40	3.39
15	SRHT	XY	104.4	0.51	5.94
15	SRHT	XZ	202.8	0.35	5.42
15	HIP	XY	146.6	0.51	5.95
15	HIP	XZ	248.9	0.39	1.80
30	SRHT	XY	80.5	0.52	3.23
30	SRHT	XZ	175.2	0.34	5.26
30	HIP	XY	113.8	0.54	3.34
30	HIP	XZ	277.5	0.42	4.69

investigated porosity when recycling SS316L powder, where it was found that recycling only resulted in slight changes to part density [21]. However, in this research, as expected, porosity was marginally greater within the SRHT samples than the equivalent HIP samples, but the difference is not discernible. It is important to note that these values are indicative and ideally, porosity volume fraction data would be provided via X-ray computed tomography (XCT).

Fig. 12 shows a selection of the porosity images taken of PBF-LB/M SS316L at varying levels of powder recycling and post processing conditions. The pores in the SRHT samples are prone to being more angular whereas, the HIP material, although containing pores, shows them to be generally spherical and less angular. As such, even though HIP may not be fully successful in removing all porosity, it appears to have removed some of the unfavourable porosity geometries that would be most damaging. The 30 sieves HIP is shown to have significantly more porosity than the other two HIP samples. As the porosity has increased within recycled material, the HIP process has not been capable of fully removing all remaining pores. In each figure, the images were captured on polished unetched surfaces, yet the final stage of the polishing procedure using OPS suspension has partially etched the surface revealing some microstructural detail.

3.2.1.3. Composition. Earlier it was shown that the oxygen content within powder particles increased with recycling and was predominantly located within surface oxides that were rich in both Mn and Si. The chemistry of solidified parts manufactured with near virgin and recycled powder were also measured to identify whether the changes in powder chemistry translated in to the chemistry of the final LPBF manufactured component.

As given in Table 7, the composition of recycled powder parts across the majority of elements did not vary significantly as powder recycling increased. As the powder feedstock remained consistent throughout,

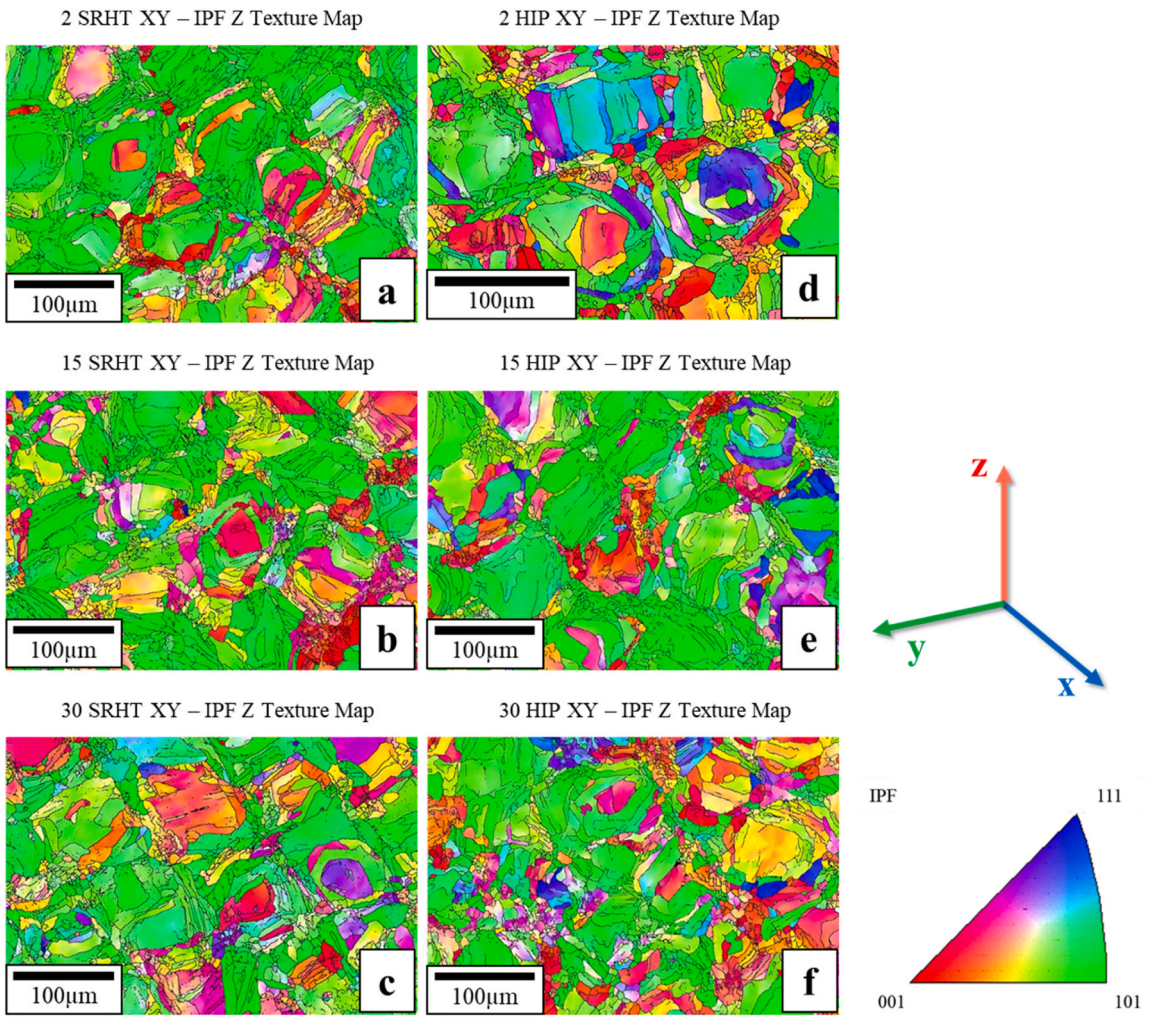

Fig. 11. Inverse pole figure maps, orientated in the Z direction perpendicular to the build direction, of SRHT and HIP samples at all levels of powder recycling in the XY orientation showing a more equiaxed morphology perpendicular to the build direction.

Table 6
Volume fractions of porosity recorded from cross sections of samples of different post processing and powder recycling levels.

Sample	Porosity (%)	Maximum Pore Size (µm^2)
2 Sieves SRHT XY	0.02 %	134.98
2 Sieves SRHT XZ	0.01 %	418.48
2 Sieves HIP XY	0.01 %	200.61
2 Sieves HIP XZ	0.04 %	45.44
15 Sieves SRHT XY	0.03 %	278.19
15 Sieves SRHT XZ	0.04 %	354.70
15 Sieves HIP XY	0.04 %	48.36
15 Sieves HIP XZ	0.04 %	48.37
30 Sieves SRHT XY	0.08 %	645.59
30 Sieves SRHT XZ	0.07 %	447.79
30 Sieves HIP XY	0.04 %	296.46
30 Sieves HIP XZ	0.08 %	73.57

there is no occasion in the PBF-LB/M process where major contamination of metallic elements could occur. The nitrogen content of manufactured parts did not vary from 670 to 680 ppm, a similar level to what was observed within the powder. Therefore, the manufacture of PBF-LB/M components and subsequent HIP operations within a nitrogen atmosphere have not contributed to a pickup of nitrogen within the microstructure. The oxygen content only increased slightly, but all values lay between 320 and 340 ppm. This is contrary to the increase of 10 % observed within the recycled powder as reported earlier.(Table 8)

3.2.2. *Mechanical properties*

As shown earlier, the changes to SS316L powder have included a coarsening of the PSD, increase in powder flowability and increase in oxygen content as the powder was recycled from 2 sieves to 15–30 sieves. An extensive series of mechanical tests and analysis were subsequently performed on samples manufactured at these points, to identify any changes to part properties as a result of the changes to the powder characteristics. These samples were also prepared in the SRHT and HIP condition.

3.2.2.1. Low cycle fatigue results. For all samples in the SRHT and HIP conditions across each of the three recycling levels, no major difference in fatigue lives were observed (Fig. 13a)). For the SRHT condition, the variation in fatigue performance between the three different recycling levels was extremely low, as shown by the R^2 value of 0.98. Therefore, the fatigue behaviour of SRHT samples appear to be insensitive to recycling level. For the HIP samples, the variation is not quite as small but still relatively low with an R^2 value of 0.92. This slight drop in consistency is driven by the samples from the 2 sieves condition. At three of the four strain values tested, these samples exhibited the worst fatigue life of any specimen type, yet the best at $\varepsilon_a = 0.6$ %. At higher strain amplitudes (>0.6 %), the power curve trendlines for SRHT and HIP samples begin to drift apart so the SRHT samples appear to have superior lives. This variation is not considerable and across the range of strains investigated, it does not appear to be significant.

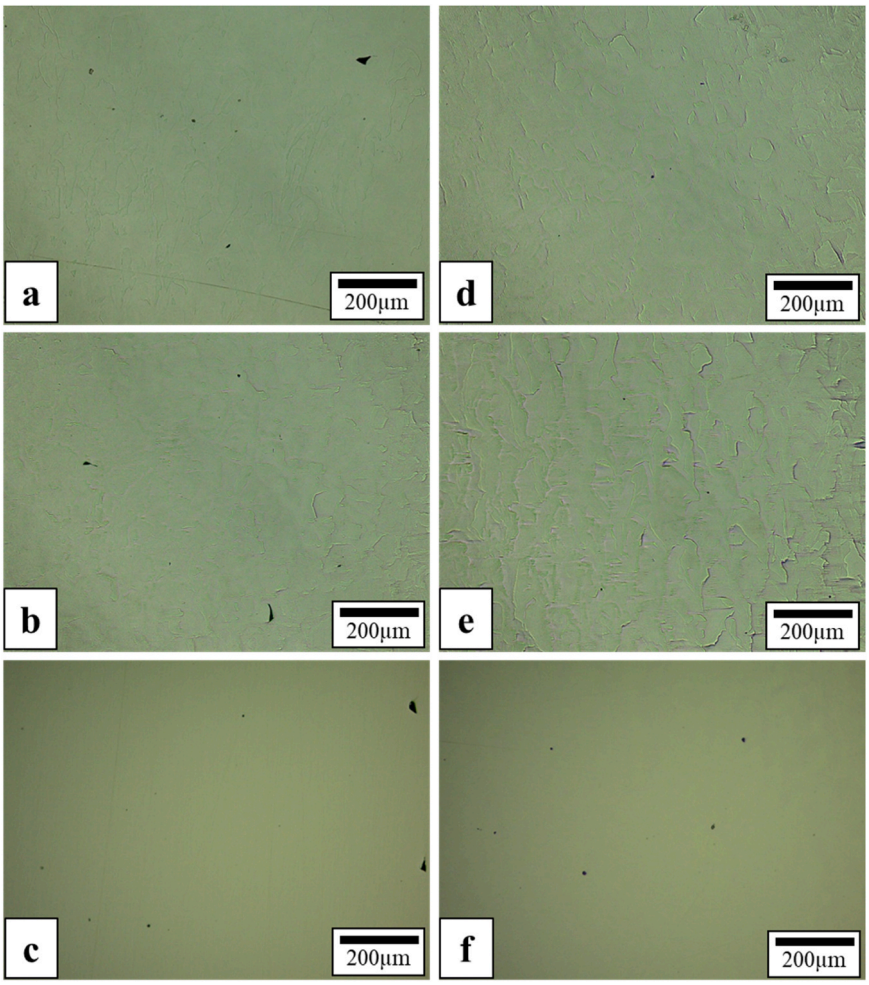

Fig. 12. Images of porosity within the XZ plane for samples of varying powder recycling level and post processing condition. a) 2 sieves SRHT b) 15 sieves SRHT c) 30 sieves SRHT d) 2 sieves HIP e) 15 sieves HIP and f) 30 sieves HIP.

Table 7
Elemental composition of PBF-LB/M SS316L samples of differing powder recycling and post processing.

Element	2 Sieves SRHT	2 Sieves HIP	15 Sieves SRHT	15 Sieves HIP	30 Sieves SRHT	30 Sieves HIP
Cr (wt %)	17.2	16.8	17.4	16.7	16.7	17.2
Ni (wt %)	12.4	12.5	12.5	12.5	12.5	12.5
Si (wt %)	0.6	0.5	0.6	0.5	0.5	0.6
Mn (wt %)	1.2	1.2	1.3	1.2	1.2	1.2
Cu (wt %)	0.04	0.02	0.03	0.02	0.02	0.02
Mo (wt %)	2.4	2.4	2.5	2.4	2.4	2.4
Al (wt %)	0.05	0.05	0.05	0.05	0.05	0.05
Fe (wt %)	66.0	66.4	65.7	65.7	66.6	66.0
C (wt%)	0.02	0.01	0.01	0.01	0.02	0.01
S (wt%)	0.003	0.003	0.003	0.003	0.003	0.003
N (ppm)	670	680	680	680	680	670
O (ppm)	320	330	320	330	340	330

The corresponding stabilised stress range behaviour for the different samples is presented in Fig. 13b). Similar to the strain amplitude plot in Fig. 13a), the S-N curves for the SRHT and HIP samples at the three different levels of powder recycling show minimal variation in fatigue performance. The R^2 values are again very high (0.98–0.99) and indicate that the recycling level has no measurable impact on the fatigue performance of the material, regardless of post processing. This also suggests that powder recycling did not generate defects within the material, either as porosity or oxides, that were of a sufficient size that they may negatively affect the fatigue performance. The most clear difference between the HIP and SRHT samples is the superior response of the SRHT material, where the SRHT samples achieve a consistently higher level of stress. This indicates that despite the HIP operation being employed to remove critical defects, this may in fact be unnecessary and further reinforces the theory that any process-induced defects are having no discernible impact on the cyclic properties.

Monotonic and stabilised hysteresis stress-strain loops were also generated across the different sample types. As shown in Fig. 14, there appears to be no clear difference in the maximum or minimum stress values achieved in the SRHT samples. The 2 sieves SRHT sample does achieve a lower yield stress (approximately 50 MPa lower) compared to the other samples, but the Young's modulus across the three material types is not affected, with values of 202 GPa, 214 GPa and 192 GPa recorded across the 3 recycling points, respectively. Despite the difference in yield properties, this is only noticeable on the first cycle, as once the material reaches the stabilised condition, the loops are perfectly aligned with negligible difference between the three data sets in terms of

Table 8
Tensile properties for SRHT and HIP samples at the three stages of powder recycling.

Sample	0.2 % Proof Stress (MPa)			Ultimate Tensile Stress (MPa)			Young's Modulus (GPa)			Strain to Failure (%)		
	Avg	*Min*	*Max*	*Avg*	*Min*	*Max*	*Avg*	*Min*	*Max*	*Avg*	*Min*	*Max*
2 SRHT	447	446	447	663	661	665	161	145	177	39.6	38.0	44.2
2 HIP	379	377	380	638	638	639	144	135	151	46.1	43.9	50.0
15 SRHT	447	445	449	668	664	670	174	171	180	66.1	62.3	73.2
15 HIP	375	371	379	636	632	640	180	161	192	70.4	67.0	72.1
30 SRHT	443	441	444	664	662	665	194	186	209	61.7	61.0	63.8
30 HIP	376	373	378	637	635	640	181	171	197	61.7	43.2	71.1

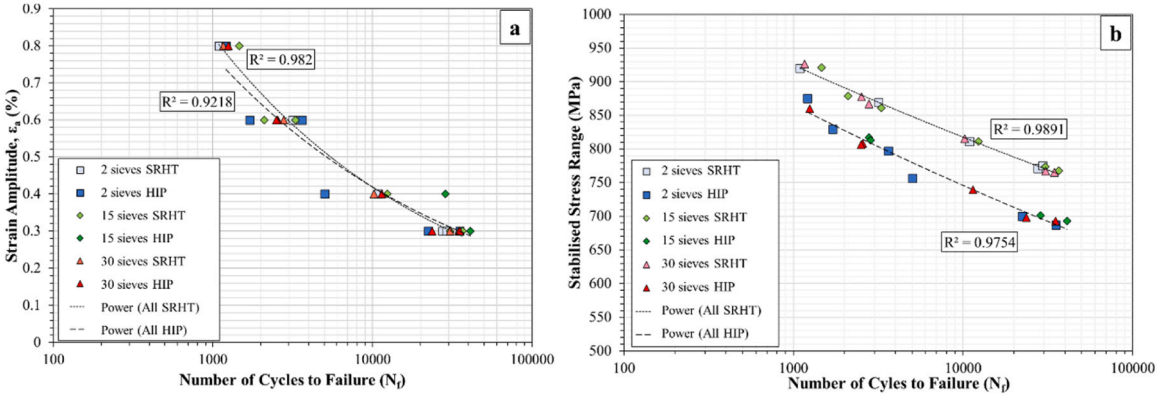

Fig. 13. Low cycle fatigue results for PBF-LB/M SS316L samples a) Strain amplitude plotted against cycles to failure, b) Stabilised stress range plotted against cycles to failure.

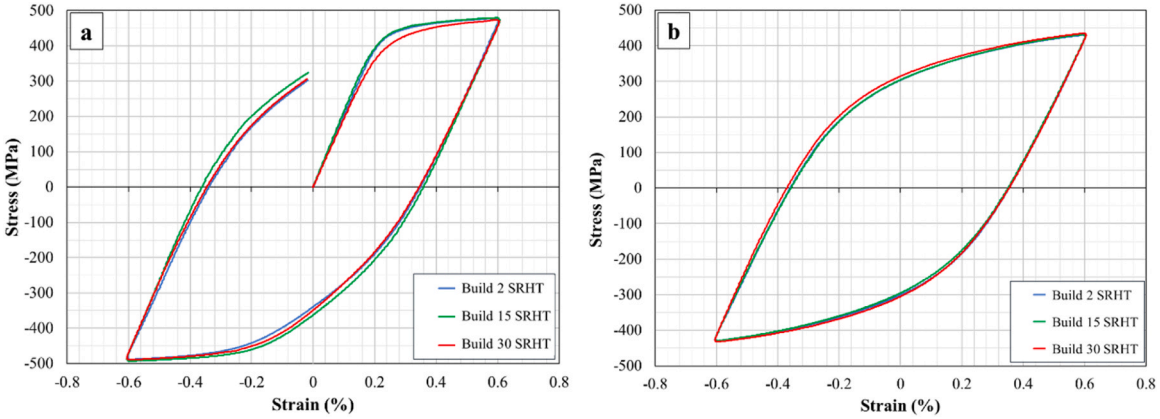

Fig. 14. a) Monotonic and b) stabilised stress-strain loops for SRHT samples at each of the three recycling levels, at ε_a=0.6 %.

the modulus, yield, cyclic softening and extent of plasticity.

The hysteresis stress-strain response of the HIP samples are presented in Fig. 15 and in a similar manner to the SRHT samples, show that there is minimal difference in the loops as the powder feedstock becomes more recycled. Unlike the monotonic loops for the SRHT samples, no discernible difference is noticeable in the yield behaviour of the three samples during the first loading cycles. Likewise, this is also true for the stabilised cycles, where the tested samples with three different levels of recycling show no difference in their stress-strain response.

When comparing the hysteresis response of the HIP material to the SRHT samples, the main observation is the difference in the level of cyclic softening that occurs. Whereas the HIP material exhibits minimal softening, the SRHT material softens by approximately 40 MPa across each of the three recycled samples once they reach their respective stabilised conditions.

Post test fractography was carried out on a selection of the samples to identify whether any discernible differences could be detected as a result of the different powder recycling levels and post processing methods. Fig. 16 shows comparative fracture surfaces for SRHT and HIP samples tested at the same powder recycling level (2 sieves) and maximum ε_a (0.6 %). As shown, the bulk fracture surfaces (Fig. 16a) and b)) are similar between the two samples, although the overload zone is more clearly defined in the HIP sample. There is also evidence of more bulk deformation in the SRHT sample, suggesting a higher level of ductility, a behaviour that is also seen later when the tensile behaviours are discussed (Section 3.2.2.2). Both samples failed from surface initiation sites, which was consistent for all the samples tested, regardless of post processing method or powder recycling level. The lack of sub surface initiation indicates that the porosity or other defects within the samples were never of a size to be deemed sufficient enough to facilitate initiation from such types of features.

The initiation zones for these samples are shown at higher magnification in Fig. 16c) and d). The images show a variation in surface elevation as the crack propagates and both have several circular

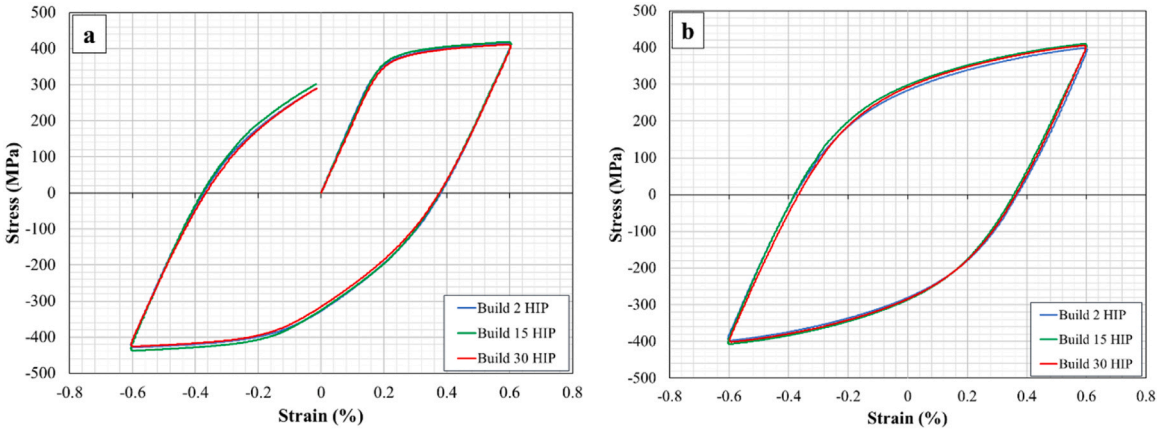

Fig. 15. a) Monotonic and b) stabilised stress-strain loops for HIP samples at each of the three recycling levels, at ε_a=0.6 %.

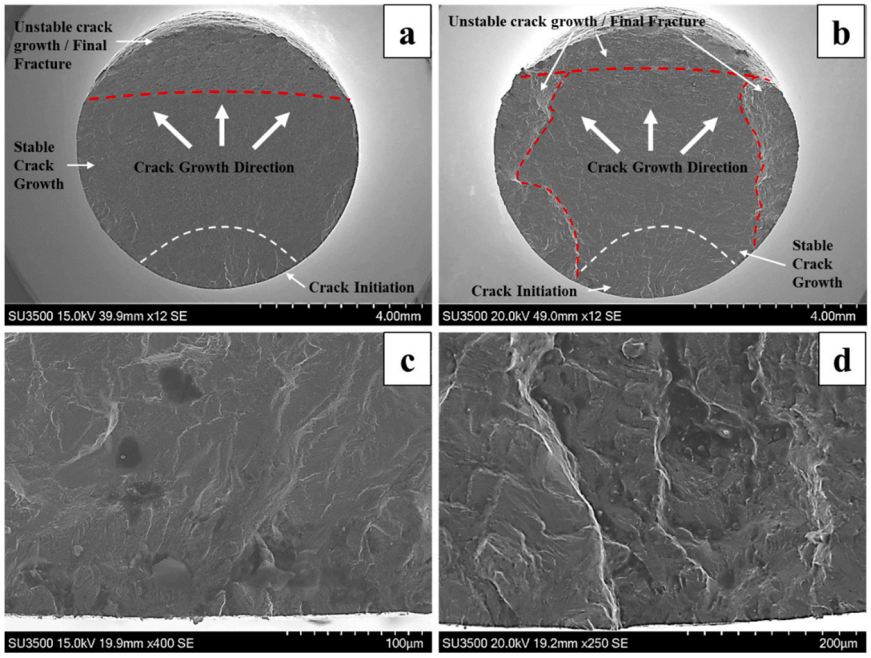

Fig. 16. SEM fractographic images of PBF-LB/M SS316L LCF samples tested at ε_a=0.6 % a) HIP sample manufactured with 2 sieves powder, b) SRHT sample manufactured with 2 sieves powder, c) initiation zone of HIP sample, d) initiation zone of SRHT sample.

particles present around the crack path. Dark spots, likely oxides, are also present on the samples. However, it is unclear whether these oxides have formed pre or post fracture. The circular particles visible are in the same size range (10–20 µm) and could potentially be resultant of fine powder that has not fully fused. These particles often appear along the line of crack propagation, suggesting that they may accelerate this stage

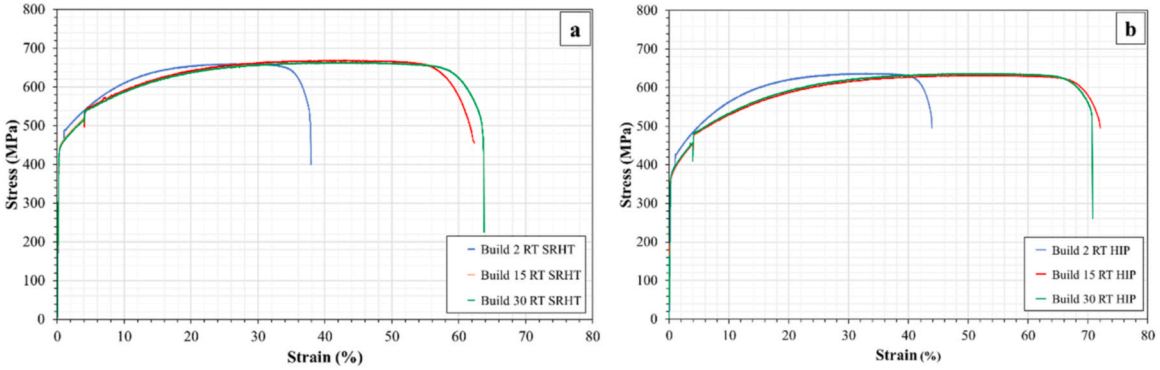

Fig. 17. Tensile stress-strain plots for a) SRHT and b) HIP samples at each of the three recycling levels.

of crack growth. Shortly after, striations become visible within the sample and the prevalence of powder particles on the fracture surface drops, indicating they may be more impactful in the earlier stages of fatigue crack growth.

3.2.2.2. Tensile results. Tensile tests were completed on samples from all three levels of powder recycling and in both post processing conditions. Fig. 17 presents the typical response for each of the six variants and indicate that the majority of tensile properties were found to be insensitive to powder recycling level, irrespective of the post-processing condition. Based off three tensile tests performed on samples from each of the six conditions, the results revealed that UTS does not vary with powder recycling level, but is generally greater for the SRHT samples (average of 665 MPa) than the HIP samples (average of 637 MPa). This increase in UTS is also reflected in the proof stress behaviour, which was also insensitive to powder recycling but saw the SRHT samples outperform HIP by approximately 70 MPa. On the contrary, strain to failure was generally found to be greater in the HIP samples [41], as would be expected given the slightly coarser grain size in this material, as has also been found previously [16].

In the SRHT samples, other factors such as large internal stresses and dislocation density may also be positively affecting the proof stress alongside the more refined grain morphology. However, other investigations of PBF-LB/M SS316L show an improvement in elongation to failure values as well as better yield strength [42,43]. This can not be explained solely by the Hall-Petch relationship which would expect a decrease of the elongation to failure. Therefore, other factors such as process-induced defects including porosity need consideration. Li et al. [44] reported that ductility in small build structures are particularly sensitive to built-in flaws, despite a high material density (> 99 %), as also seen here. Another factor is the presence of deformation twins, which shall be discussed later.

As powder recycling increases, the Young's modulus of samples also increased, by 35 GPa from the 2 sieves to 30 sieves condition in the SRHT material, and by 27 GPa from 2 sieves and 30 sieves for the HIP condition.

Unlike proof stress and UTS, strain to failure was generally found to be more sensitive to the level of powder recycling. Fig. 18 presents the fracture behaviours of two of the SRHT samples; after 2 powder recycle sieves and 30 sieves. EBSD was employed to calculate the quantity of deformation twins in the two samples, since previous studies have identified twinning deformation as a major contributor to an increased ductility within PBF-LB/M SS316L [42,43,45]. Previously, Pham et al. [43] found that the small cellular structure of PBF/LB-M SS316L resulting from rapid cooling and dense dislocations contributed significantly to the high yield strength observed in the material, typically nearly twice that of the annealed equivalent. In their study, the presence of twinning induced plasticity was believed to be the main factor for the enhanced ductility of the material despite a relatively high volume of porosity. Pham et al. attributed the twinning behaviour to the presence of nitrogen gas in the manufacturing process, since nitrogen has the ability of reducing the stacking fault energy of the material, thereby causing dislocations to disassociate and subsequently facilitating deformation twinning. This twinning mechanism results in substantial plasticity during deformation, which can offset the adverse impact of porosity [43].

To understand the twinning behaviour of the materials in the current study, EBSD maps were recorded approximately 1 mm away from the fracture surface to achieve a balance between scanning a highly deformed area while also being able to scan effectively, as the success rate of an EBSD scan can drop significantly when there is a high degree of deformed cells. In the analysis, twins were classed as any boundary with an angle between 59 ° and 61 ° to account for imprecision within the EBSD scan. From this, it was found that the twin percentage increased slightly from undeformed material and also increased with the level of powder recycling. The overall increase was not significant with

Table 9
Twin boundary percentages in undeformed and deformed PBF-LB/M SS316L from tensile tests.

Sample	% Twins (59°-61°)
Undeformed PBF-LB/M SS316L	0.19–0.24 %
2 sieves fracture zone	0.9 %
15 sieves fracture zone	1.2 %
30 sieves fracture zone	1.3 %

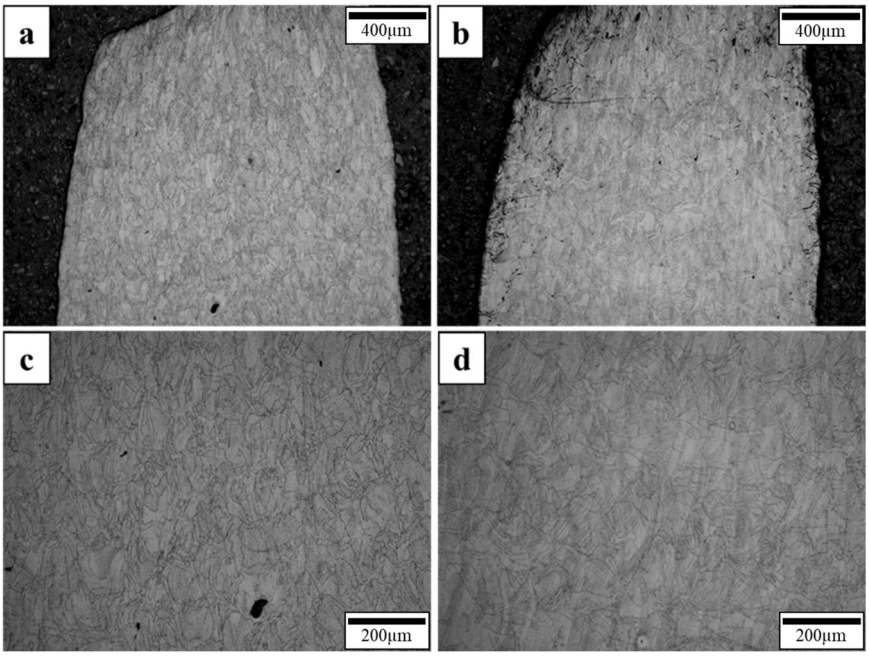

Fig. 18. SEM micrographs of the deformed microstructures of SRHT PBF-LB/M SS316L after tensile testing a) 2 sieves sample, b) 30 sieves sample, c) 2 sieves sample (higher magnification), d) 30 sieves sample (higher magnification).

twins only contributing to a maximum of 1.3 % of the grain boundaries, as presented in Table 9. This suggests that twinning deformation is taking place to a limited extent during tensile testing, but that it is unlikely to be the main factor contributing towards the high strain to failure values recorded after 15 and 30 sieves.

3.2.2.3. Impact results. The results from three Charpy impact tests on SRHT and HIP samples from three different levels of powder recycling are presented in Fig. 19. The results show that no trends exist between the energy absorbed and recycling level, after either type of post processing procedure. The impact energies for SRHT samples are almost identical at every level of recycling, however, scatter within these measurements increases slightly with powder recycling. This trend is not represented within the HIP samples, where the range of results is minimal for all levels of powder recycling. There is a slight decrease in the impact energy of HIP samples between BP1 at 2 recycles and BP2 at 15 recycles. This drop of approximately 9 % is not repeated between BP2 and BP3 (30 recycles). Lou et al. have previously identified a drop in the impact energy of SS316L when additively manufactured due to the presence of Si rich oxide particles [36]. Particles of similar chemistry have been seen to increase in recycled powder within this study. However, if these particles were responsible for a drop in impact energy with powder recycling, it might be expected that the decrease in impact energy would be present in the SRHT condition as well as the HIP, which did not occur.

There is a significant difference in the impact toughness of SRHT and HIP samples. At BP1, BP2 and BP3, the impact energy of SRHT samples is 28 %, 36 % and 36 %. SRHT samples consistently achieved higher impact energies than the HIP samples, indicating a higher level of toughness properties. This level of variation suggests that some level of microstructural variation is responsible for the improved performance of SRHT samples.

When comparing the fracture surfaces of each of the impact samples (Fig. 20), the SRHT sample exhibits far more angular faceted features that are more typical of a brittle fracture. In comparison, although the HIP bulk surface is less rough, higher magnification images shows more unevenness of the surface. The HIP samples, particularly at higher magnification, show evidence of faceted features that are more typical of a brittle fracture. Greater ductility is generally associated with greater toughness energy in impact testing. But, for SRHT samples to require greater fracture energy while also showing lower potential ductility requires them to have a higher overall strength. This trade-off is possible with the finer grain size of SRHT samples.

3.2.3. Corrosion properties

Due to the aggressive marine environment that PBF-LB/M SS316L parts can be exposed to in service, it is important to consider how the corrosion properties of the material may be affected by powder recycling. In order to characterise these properties, cyclic polarisation tests in 3.5 %NaCl were performed to identify the variation in corrosion properties associated with parts manufactured with recycled powder.

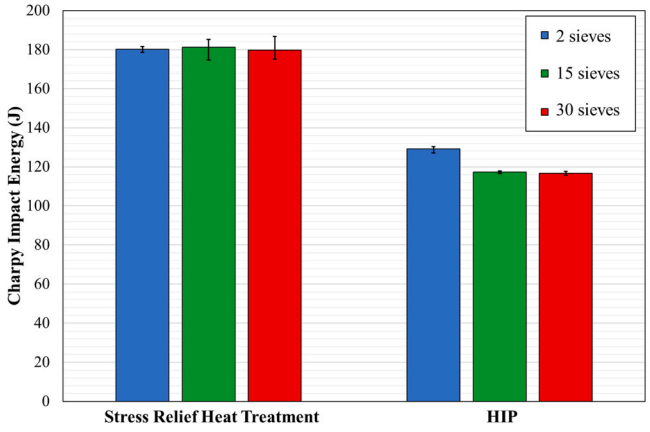

Fig. 19. The average Charpy impact energies of samples manufactured with 2 sieves, 15 sieves and 30 sieves powder, in the SRHT and HIP conditions.

SRHT samples were tested in both the 2 sieves and 30 sieves condition to identify the variation to corrosion performance in both extremes of the recycling spectrum. Cyclic polarisation curves for SRHT samples are somewhat consistent, even between the 2 sieves and 30 sieves condition (Fig. 21a)). Pitting potential for all samples sit between 1.0 V and 1.1 V, regardless of recycling level. Re-passivation above the E_{corr} only occurs in one sample which was manufactured with fresher powder at 2 sieves. The E_{corr} itself was typically around −0.15 V; the consistency of this value suggests that the initial protective barrier oxide formed on SRHT samples was uniform and similar across multiple samples. However, the passive current densities of the SRHT samples after 2 sieves exhibit a difference of around two orders of magnitude (or 100 times). This infers that if the oxide layer breaks down and pitting starts, the pit current density could potentially be 100 times greater in some samples as compared to others, and therefore the rate to corrosion damage could be considerably quickly.

Similarly to the SRHT samples, HIP samples displayed excellent consistency within cyclic polarisation curves. The pitting potential of samples lay between 0.4 and 0.5 V, which is lower than the SRHT material (Fig. 21b)). The values of E_{corr} sat around −0.15 V which was similar to the SRHT material. Metastable pitting was far more prevalent among all HIP samples but the point of E_{pit} is difficult to determine for two samples (2 Sieves 3 and 30 sieves 1). Both of these samples pitted but then stabilised at a lower current density.

Overall, PBF-LB/M SS316L was shown to be consistent in terms of E_{corr} and E_{pit}. Pitting potential was generally greater in PBF-LB/M material, with previously analysed wrought samples having a pitting potential of 0.33 V to 0.46 V, HIP at 0.40 V to 0.46 V and SRHT at 1.03 V to 1.15 V (as given in Table 10). It has previously been reported that wrought samples of SS316L are liable to contain MnS precipitates that do not form within PBF-LB/M 316 L due to the faster cooling rates present [46]. These MnS precipitates are preferential sites for pitting corrosion to occur and therefore can reduce the pitting potential of wrought material over PBF-LB/M samples [47]. The quantity of chromium within the passive layer of SS316L has also been reported to be greater for PBF-LB/M material than wrought samples, thus also improving corrosion resistance [48]. These factors help to explain the improved performance of PBF-LB/M material over wrought in terms of E_{pit}.

The competitive and consistent values of E_{pit} also indicate good densification of the PBF-LB/M SS316L material, since the pitting potential of PBF-LB/M has been shown to be sensitive to porosity within the sample. Grech et al. identified a difference in the pitting potential of HIP PBF-LB/M SS316L from between 0.2 and 1.0 V, which was driven significantly by the presence of porosity [49]. Sander et al. determined that the effect of porosity on the pitting potential of SS316L is negligible when a porosity volume fraction below 0.4 % is achieved [47], as was also seen within this study. Therefore, this highly densified structure reduces the impact of porosity on pitting potential.

The lack of variation in pitting potential after different levels of powder recycling indicates that any changes within the samples, either within the chemistry or porosity due to powder recycling, were not significant enough to affect a change in corrosion performance. However, the pitting potential was superior within the SRHT condition than in HIP material. Although porosity is expected to be less within the HIP material, the density of the SRHT material appears sufficient so that pore size did not majorly inhibit the performance of the material. As porosity and chemical changes are unlikely to be the cause of increased E_{pit} values in the SRHT material, microstructural variations are suggested to be the main driver for the difference. Grain boundaries in SS316L are richer in chromium and therefore their increased prevalence improves

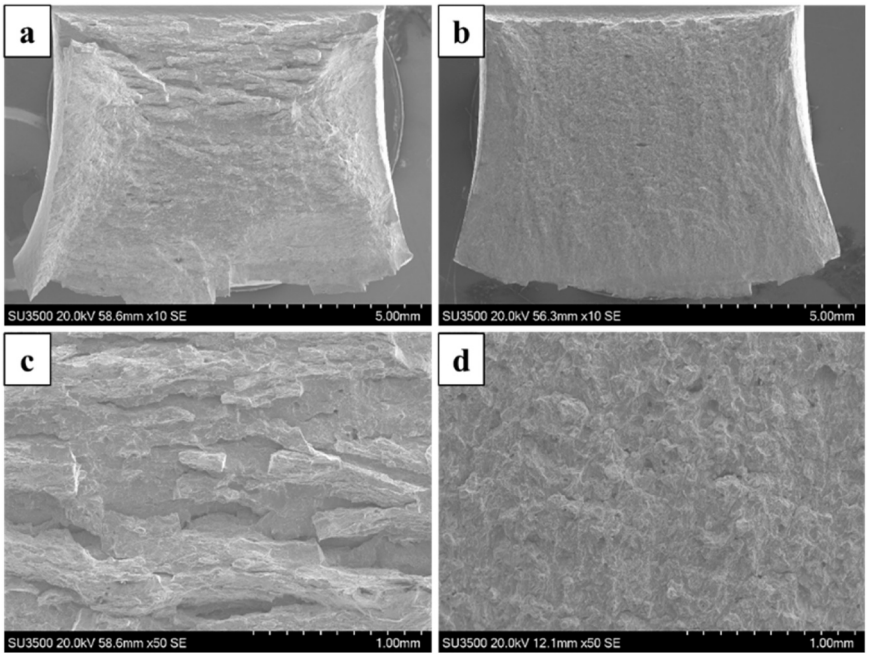

Fig. 20. Charpy impact fracture surfaces for PBF-LB/M SS316L samples manufactured with 2 sieves powder a) SRHT fracture surface, b) HIP fracture surface, c) faceted features on the SRHT fracture surface, d) cracking, pores on the HIP fracture surface.

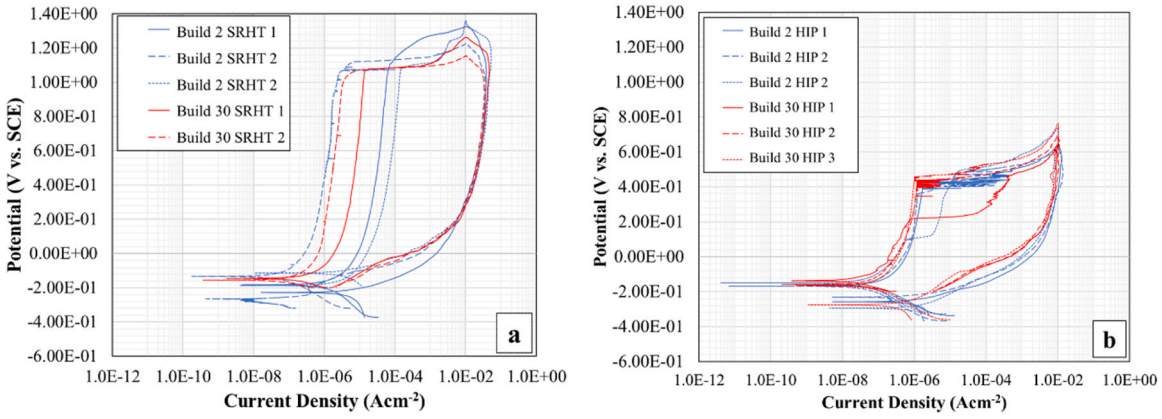

Fig. 21. Cyclic polarisation curves for PBF-LB/M SS316L after 2 sieves and 30 sieves in **a)** SRHT and **b)** HIP conditions.

Table 10
A summary of cyclic polarisation results for all samples. *Only taken from one value.

Sample	E_{corr} (V)	E_{pit} (V)	E_{rep} (V)
Wrought	-0.08 to −0.18	0.33–0.46	-0.10 to −0.27
2 Sieves SRHT	-0.13 to −0.19	1.08–1.15	-0.09 to -0.24
2 Sieves HIP	-0.15 to −0.17	0.40–0.46	-0.23 to −0.28
30 Sieves SRHT	-0.15 to −0.16	1.03–1.08	N/A
30 Sieves HIP	-0.14 to −0.16	0.44–0.46	-0.26*

the distribution of chromium and molybdenum across the alloy surface. The more even distribution of elements is important for corrosion resistance and this has been shown to improve the stability of the protective oxide layer [50]. This is also supported by the increased amount of metastable pitting in HIP samples where the oxide layer was temporarily breached more often than in SRHT samples prior to failure.

4. Summary

In general, the microstructure, mechanical properties and chemistry of PBF-LB/M SS316L were unaffected by the use of recycled powder. Despite the evolution of powder properties, the knock-on effects on the mechanical behaviour were not significant. Overall, this is a positive outcome for the further reuse of SS316L powder in a production setting.

SRHT samples were observed to have a superior mechanical behaviour compared to the HIP material across the majority of mechanical performance metrics. Microstructural analysis identified finer grain sizes and slightly greater anisotropy and texture within the SRHT samples compared to HIP material. The HIP process was conducted at 1150 °C compared to 700 °C for the SRHT. At this increased temperature, recrystallisation and grain growth are possible, which results in less anisotropy and lower texture, but grain growth leads to larger grain sizes. The overall effect of this saw a reduction in the UTS, proof stress and LCF S-N behaviour in the HIP material, as a result of the Hall-Petch relationship.

The LCF performance of PBF-LB/M SS316L was seen to be extremely stable in terms of fatigue lives and stress ranges, which resulted in an

almost identical S-N behaviour for different levels of powder recycling. The remaining variation can confidently be attributed to scatter associated with the test arrangement and typical material variance. The similar fatigue performance with differing levels of powder recycling is firstly due to the lack of microstructural variation present from using recycled powder. In terms of grain size, anisotropy and texture, powder recycling was not observed to have any significant effect. Secondly, low porosity was observed across all samples, regardless of powder recycling or post processing method. Fractographic images showed that all fatigue failures were surface initiated and that defects within the material, if and when present, were not significant enough in size to encourage subsurface initiation or to accelerate fatigue crack growth. The critical defect size for SS316L has been shown to be heavily dependent on the defect location with surface initiations being far more significant for the fatigue life of specimens [51]. The high ductility of 316 L also make it insensitive to internal defects in regards to fatigue life. Although porosity was seen to increase in samples manufactured with recycled powder, it did not reach a point where it had a substantial effect on fatigue behaviour as the maximum pore size only increased marginally. Porosity was observed to typically be more angular and larger within SRHT material, yet despite this, a negative influence on the fatigue performance did not occur. The consistently low porosity also resulted in highly repeatable results during cyclic polarisation corrosion testing. SRHT and HIP samples were also competitive or outperformed wrought material in regards to their E_{pit} values. The superior pitting potential for the SRHT samples was attributed to the favourable distribution of Cr at grain boundary locations.

The tensile performance of PBF-LB/M SS316L was also mainly unaffected by the change in powder recycling level. UTS and yield strength were not changed at all, yet both strain to failure and Young's modulus saw increases with powder recycling. With Young's modulus, there was a small steady increase with powder recycling level and strain to failure saw a large increase for some samples after powder recycling. The difference in the ductility properties has been proposed to be attributed to the small amount of twinning within the material, that was not present in the samples prior to deformation. Twinning deformation can lead to excellent ductility within PBF-LB/M SS316L [42,45], but the overall increase in twin boundaries was relatively small, rising from 0.9 % to 1.3 % from 2 sieves to 30 sieves material. Although this slight increase may have helped with greater deformation, it may also just be a result of the increased deformation within samples manufactured with recycled powder. As a result, it can not be used to conclusively explain the changes that occurred in recycled powder samples.

The larger grain size of the HIP samples was also associated with a drop in mechanical strength and this was seen in both the fatigue and tensile experiments. The tensile results displayed the typical Hall-Petch relationship of increasing strength and decreasing ductility for the SRHT samples as the grain size decreased. The grain size differences also agree with the findings from the cyclic polarisation and Charpy impact testing. The increase in isotropy, seen in the HIP samples, may be desirable for reducing the difference in performance between vertically and horizontally orientated samples, but overall, the SRHT samples offered a superior mechanical performance.

Conclusions

This study consisted of understanding the influence of powder recycling on the mechanical and corrosion properties of PBF-LB/M SS316L. From this research, the following conclusions can be drawn:

- The physical and chemical properties of SS316L metallic powder was found to change during the recycling procedure. The PSD was seen to coarsen by approximately 5 μm after 30 recycles, which subsequently led to an increase in powder flowability due to a reduction of fine particles, particularly in the <20 μm range.
- The oxygen content of recycled powder increased by approximately 10 % after 30 recycles. The oxygen was predominantly located within oxides on the surface of spatter particles in manganese and silicon rich oxides. The rate of oxygen accumulation in powder particles was linear with the amount of sieving of the powder.
- The ferrite content was shown to increase slightly with powder recycling. However, these changes were small and not deemed significant enough to create any visible knock-on effects on the mechanical properties of fully fused material.
- Limited microstructural changes were identified in PBF-LB/M SS316L as a result of using recycled powder. This included grain size, texture and phase composition. The lack of microstructural variation and low porosity in the final material containing recycled powder resulted in no effect of powder reuse on the low cycle fatigue performance of PBF-LB/M SS316L. The low variation in porosity also meant that powder recycling did not affect the pitting potentials of 316 L parts as determined from cyclic polarisation studies.
- The tensile strength and yield strength properties of PBF-LB/M SS316L were not affected by powder reuse. Yet, ductility increased in parts with recycled powder, potentially aided by limited deformation twinning but predominantly driven by low porosity in the samples.
- The more significant influence on the mechanical and corrosion behaviour of recycled PBF-LB/M SS316L material was the post-processing procedure. Whereas the HIP operation employed was designed to reduce or eliminate any process-induced defects such as lack of fusion and porosity, this was found to be unnecessary given the comparable density found in material that was not subjected to HIP. Indeed, given that the HIP procedure was performed at a temperature in excess of the material's solution temperature, this inadvertently led to a larger degree of grain growth, as opposed to the stress relief heat treatment performed at 700 °C. Thus, the HIP process coarsened the microstructure, leading to a subsequent reduction in the tensile strength and LCF properties of the material.

CRediT authorship contribution statement

Nicholas Barnard: Investigation, Data curation. **Rory Douglas:** Writing – original draft, Methodology, Investigation, Formal analysis, Data curation. **Nicholas Lavery:** Validation, Methodology, Formal analysis. **Thomas Jones:** Supervision, Project administration, Methodology, Investigation, Funding acquisition, Conceptualization. **James Sullivan:** Validation, Methodology, Data curation. **Robert Lancaster:** Writing – original draft, Supervision, Resources, Project administration, Methodology, Investigation, Funding acquisition, Conceptualization.

Declaration of competing interest

The authors declare that they have no known competing financial interests or personal relationships that could have appeared to influence the work reported in this paper.

Data availability

The data that has been used is confidential.

Acknowledgements

The current research was funded under the EPSRC Industrial Case Award EP/T517537/1. The provision of a research bursary, materials, and supporting information from Rolls-Royce plc. is gratefully acknowledged. Mechanical tests were performed at Swansea Materials Research and Testing Ltd. (SMaRT).

References

[1] N. Guo, M.C. Leu, Additive manufacturing: technology, applications and research needs, Front. Mech. Eng. vol. 8 (3) (Sep. 2013) 215–243, https://doi.org/10.1007/s11465-013-0248-8.

[2] M. Marrey, E. Malekipour, H. El-Mounayri, E.J. Faierson, A framework for optimizing process parameters in powder bed fusion (PBF) process using artificial neural network (ANN), Procedia Manuf. vol. 34 (2019) 505–515, https://doi.org/10.1016/j.promfg.2019.06.214.

[3] M. Zhang, et al., Fatigue and fracture behaviour of laser powder bed fusion stainless steel 316L: influence of processing parameters, Mater. Sci. Eng. A vol. 703 (Aug. 2017) 251–261, https://doi.org/10.1016/j.msea.2017.07.071.

[4] A. Leicht, M. Rashidi, U. Klement, E. Hryha, Effect of process parameters on the microstructure, tensile strength and productivity of 316L parts produced by laser powder bed fusion, Mater. Charact. vol. 159 (Jan. 2020) 110016, https://doi.org/10.1016/j.matchar.2019.110016.

[5] R. Magana-Carranza, C.J. Sutcliffe, E.A. Patterson, The effect of processing parameters and material properties on residual forces induced in laser powder bed fusion (L-PBF), Addit. Manuf. vol. 46 (Oct. 2021) 102192, https://doi.org/10.1016/j.addma.2021.102192.

[6] U. Scipioni Bertoli, B.E. MacDonald, J.M. Schoenung, Stability of cellular microstructure in laser powder bed fusion of 316L stainless steel, Mater. Sci. Eng. A vol. 739 (Jan. 2019) 109–117, https://doi.org/10.1016/j.msea.2018.10.051.

[7] M. Laleh, et al., On the unusual intergranular corrosion resistance of 316L stainless steel additively manufactured by selective laser melting, Corros. Sci. vol. 161 (Dec. 2019) 108189, https://doi.org/10.1016/j.corsci.2019.108189.

[8] S.R. Narasimharaju, et al., A comprehensive review on laser powder bed fusion of steels: Processing, microstructure, defects and control methods, mechanical properties, current challenges and future trends, J. Manuf. Process vol. 75 (Mar. 2022) 375–414, https://doi.org/10.1016/j.jmapro.2021.12.033.

[9] R. Shrestha, J. Simsiriwong, N. Shamsaei, Fatigue behavior of additive manufactured 316L stainless steel parts: effects of layer orientation and surface roughness, Addit. Manuf. vol. 28 (Aug. 2019) 23–38, https://doi.org/10.1016/j.addma.2019.04.011.

[10] F.T. Piller *et al.*, Introducing a Holistic Profitability Model for Additive Manufacturing: An Analysis of Laser-powder Bed Fusion, in *2018* IEEE International Conference on Industrial Engineering and Engineering Management (IEEM), IEEE, Dec. 2018, pp. 1730–1735. doi: 10.1109/IEEM.2018.8607729.

[11] N.E. Gorji, R. O'Connor, A. Mussatto, M. Snelgrove, P.G.M. González, D. Brabazon, Recyclability of stainless steel (316 L) powder within the additive manufacturing process, Mater. vol. 8 (Dec. 2019) 100489, https://doi.org/10.1016/j.mtla.2019.100489.

[12] C.L.A. Leung, S. Marussi, M. Towrie, R.C. Atwood, P.J. Withers, P.D. Lee, The effect of powder oxidation on defect formation in laser additive manufacturing, Acta Mater. vol. 166 (Mar. 2019) 294–305, https://doi.org/10.1016/j.actamat.2018.12.027.

[13] A. Mussatto, R. Groarke, A. O'Neill, M.A. Obeidi, Y. Delaure, D. Brabazon, Influences of powder morphology and spreading parameters on the powder bed topography uniformity in powder bed fusion metal additive manufacturing, Addit. Manuf. vol. 38 (Feb. 2021) 101807, https://doi.org/10.1016/j.addma.2020.101807.

[14] N. Ahmed, I. Barsoum, G. Haidemenopoulos, R.K.A. Al-Rub, Process parameter selection and optimization of laser powder bed fusion for 316L stainless steel: a review, J. Manuf. Process vol. 75 (Mar. 2022) 415–434, https://doi.org/10.1016/j.jmapro.2021.12.064.

[15] A.B. Spierings, N. Herres, G. Levy, Influence of the particle size distribution on surface quality and mechanical properties in AM steel parts, Rapid Prototyp. J. vol. 17 (3) (Apr. 2011) 195–202, https://doi.org/10.1108/13552541111124770.

[16] N.P. Lavery, et al., Effects of hot isostatic pressing on the elastic modulus and tensile properties of 316L parts made by powder bed laser fusion, Mater. Sci. Eng. A vol. 693 (May 2017) 186–213, https://doi.org/10.1016/j.msea.2017.03.100.

[17] R. Douglas, R. Lancaster, T. Jones, N. Barnard, J. Adams, The influence of powder reuse on the properties of laser powder bed-fused stainless steel 316L: a review, Adv. Eng. Mater. vol. 24 (9) (Sep. 2022), https://doi.org/10.1002/adem.202200596.

[18] P. Bajaj, A. Hariharan, A. Kini, P. Kürnsteiner, D. Raabe, E.A. Jägle, Steels in additive manufacturing: a review of their microstructure and properties, Mater. Sci. Eng. A vol. 772 (Jan. 2020) 138633, https://doi.org/10.1016/j.msea.2019.138633.

[19] A. Adeyemi, E.T. Akinlabi, R.M. Mahamood, Powder bed based laser additive manufacturing process of stainless steel: a review, Mater. Today Proc. vol. 5 (9) (2018) 18510–18517, https://doi.org/10.1016/j.matpr.2018.06.193.

[20] K. Murray, M. Kearns, P. Davies, N. Lavery, and S. Brown, The Influence Of Powder Ageing Characteristics On 316L Stainless Steel Processed By Laser Based Powder Bed Fusion, in Proceedings Euro PM 2017: International Powder Metallurgy Congress and Exhibition, Milan, Italy, 2017.

[21] T. Delacroix, F. Lomello, F. Schuster, H. Maskrot, J.-P. Garandet, Influence of powder recycling on 316L stainless steel feedstocks and printed parts in laser powder bed fusion, Addit. Manuf. vol. 50 (Feb. 2022) 102553, https://doi.org/10.1016/j.addma.2021.102553.

[22] ISO 17025:2017, General Requirements for the Competence of Testing and Calibration Laboratories, ISO. 2017.

[23] 2010, ASTM E 606, Standard Practice for Strain-Controlled Fatigue Testing, Astm.

[24] 2010, ASTM E8-04, Standard Test Methods for Tension Testing of Metallic Materials, ASTM.

[25] ASTM E23–23a, Standard Test Methods for Notched Bar Impact Testing of Metallic Materials, ASTM.

[26] M.J. Heiden, et al., Evolution of 316L stainless steel feedstock due to laser powder bed fusion process, Addit. Manuf. vol. 25 (Jan. 2019) 84–103, https://doi.org/10.1016/j.addma.2018.10.019.

[27] S. Mohd Yusuf, E. Choo, N. Gao, Comparison between virgin and recycled 316L SS and AlSi10Mg powders used for laser powder bed fusion additive manufacturing, Metals vol. 10 (12) (Dec. 2020) 1625, https://doi.org/10.3390/met10121625.

[28] R. Groarke, et al., 316L stainless steel powders for additive manufacturing: relationships of powder rheology, size, size distribution to part properties, Materials vol. 13 (23) (Dec. 2020) 5537, https://doi.org/10.3390/ma13235537.

[29] 2020, ASTM B213-20, Standard Test Methods for Flow Rate of Metal Powders Using the Hall Flowmeter Funnel ASTM.

[30] P. Mellin, O. Lyckfeldt, P. Harlin, H. Brodin, H. Blom, A. Strondl, Evaluating flowability of additive manufacturing powders, using the Gustavsson flow meter, Met. Powder Rep. vol. 72 (5) (Sep. 2017) 322–326, https://doi.org/10.1016/j.mprp.2017.06.003.

[31] T. Delacroix, et al., Influence of build characteristics and chamber oxygen concentration on powder degradation in laser powder bed fusion, Powder Technol. vol. 416 (Feb. 2023) 118231, https://doi.org/10.1016/j.powtec.2023.118231.

[32] D. Galicki, et al., Localized changes of stainless steel powder characteristics during selective laser melting additive manufacturing, Metall. Mater. Trans. A vol. 50 (3) (Mar. 2019) 1582–1605, https://doi.org/10.1007/s11661-018-5072-7.

[33] C. Lu, et al., A comprehensive characterization of virgin and recycled 316L powders during laser powder bed fusion, J. Mater. Res. Technol. vol. 18 (May 2022) 2292–2309, https://doi.org/10.1016/j.jmrt.2022.03.125.

[34] M. Simonelli, et al., A study on the laser spatter and the oxidation reactions during selective laser melting of 316L stainless steel, Al-Si10-Mg, and Ti-6Al-4V, Metall. Mater. Trans. A vol. 46 (9) (Sep. 2015) 3842–3851, https://doi.org/10.1007/s11661-015-2882-8.

[35] X. Yang, F. Gao, F. Tang, X. Hao, Z. Li, Effect of surface oxides on the melting and solidification of 316l stainless steel powder for additive manufacturing, Metall. Mater. Trans. A vol. 52 (10) (Oct. 2021) 4518–4532, https://doi.org/10.1007/s11661-021-06405-3.

[36] X. Lou, P.L. Andresen, R.B. Rebak, Oxide inclusions in laser additive manufactured stainless steel and their effects on impact toughness and stress corrosion cracking behavior, J. Nucl. Mater. vol. 499 (Feb. 2018) 182–190, https://doi.org/10.1016/j.jnucmat.2017.11.036.

[37] A.T. Sutton, C.S. Kriewall, S. Karnati, M.C. Leu, J.W. Newkirk, Characterization of AISI 304L stainless steel powder recycled in the laser powder-bed fusion process, Addit. Manuf. vol. 32 (Mar. 2020) 100981, https://doi.org/10.1016/j.addma.2019.100981.

[38] F.C. Pinto, I.R. Souza Filho, M.J.R. Sandim, H.R.Z. Sandim, Defects in parts manufactured by selective laser melting caused by δ-ferrite in reused 316L steel powder feedstock, Addit. Manuf. vol. 31 (Jan. 2020) 100979, https://doi.org/10.1016/j.addma.2019.100979.

[39] D. Herzog, V. Seyda, E. Wycisk, C. Emmelmann, Additive manufacturing of metals, Acta Mater. vol. 117 (Sep. 2016) 371–392, https://doi.org/10.1016/j.actamat.2016.07.019.

[40] V. Seyda, N. Kaufmann, C. Emmelmann, Investigation of Aging Processes of Ti-6Al-4 V powder material in laser melting, Phys. Procedia vol. 39 (2012) 425–431, https://doi.org/10.1016/j.phpro.2012.10.057.

[41] B.P. Kashyap, K. Tangri, On the Hall-Petch relationship in type 316L stainless steel at room temperature, Scr. Metall. Et. Mater. vol. 24 (9) (Sep. 1990) 1777–1782, https://doi.org/10.1016/0956-716X(90)90545-R.

[42] Y.M. Wang, et al., Additively manufactured hierarchical stainless steels with high strength and ductility, Nat. Mater. vol. 17 (1) (Jan. 2018) 63–71, https://doi.org/10.1038/nmat5021.

[43] M.S. Pham, B. Dovgyy, P.A. Hooper, Twinning induced plasticity in austenitic stainless steel 316L made by additive manufacturing, Mater. Sci. Eng. A vol. 704 (Sep. 2017) 102–111, https://doi.org/10.1016/j.msea.2017.07.082.

[44] Z. Li, et al., Tensile properties, strain rate sensitivity, and activation volume of additively manufactured 316L stainless steels, Int. J. Plast. vol. 120 (Sep. 2019) 395–410, https://doi.org/10.1016/j.ijplas.2019.05.009.

[45] Md Shamsujjoha, S.R. Agnew, J.M. Fitz-Gerald, W.R. Moore, T.A. Newman, High strength and ductility of additively manufactured 316L stainless steel explained, Metall. Mater. Trans. A vol. 49 (7) (Jul. 2018) 3011–3027, https://doi.org/10.1007/s11661-018-4607-2.

[46] T. Voisin, et al., Pitting corrosion in 316L stainless steel fabricated by laser powder bed fusion additive manufacturing: a review and perspective, JOM vol. 74 (4) (Apr. 2022) 1668–1689, https://doi.org/10.1007/s11837-022-05206-2.

[47] G. Sander, A.P. Babu, X. Gao, D. Jiang, N. Birbilis, On the effect of build orientation and residual stress on the corrosion of 316L stainless steel prepared by selective laser melting, Corros. Sci. vol. 179 (Feb. 2021) 109149, https://doi.org/10.1016/j.corsci.2020.109149.

[48] M.J.K. Lodhi, A.D. Iams, E. Sikora, T.A. Palmer, Microstructural features contributing to macroscopic corrosion: the role of oxide inclusions on the corrosion properties of additively manufactured 316L stainless steel, Corros. Sci. vol. 203 (Jul. 2022) 110354, https://doi.org/10.1016/j.corsci.2022.110354.

[49] I.S. Grech, J.H. Sullivan, R.J. Lancaster, J. Plummer, N.P. Lavery, The optimisation of hot isostatic pressing treatments for enhanced mechanical and corrosion performance of stainless steel 316L produced by laser powder bed fusion, Addit.

Manuf. vol. 58 (Oct. 2022) 103072, https://doi.org/10.1016/j.addma.2022.103072.

[50] R.I. Revilla, et al., Microstructure and corrosion behavior of 316L stainless steel prepared using different additive manufacturing methods: a comparative study bringing insights into the impact of microstructure on their passivity, Corros. Sci. vol. 176 (Nov. 2020) 108914, https://doi.org/10.1016/j.corsci.2020.108914.

[51] O. Andreau, E. Pessard, I. Koutiri, P. Peyre, N. Saintier, Influence of the position and size of various deterministic defects on the high cycle fatigue resistance of a 316L steel manufactured by laser powder bed fusion, Int. J. Fatigue vol. 143 (Feb. 2021) 105930, https://doi.org/10.1016/j.ijfatigue.2020.105930.